# Near-surface dynamics of a separated jet in the coastal transition zone off Oregon

A. O. Koch,[1] A. L. Kurapov,[1] and J. S. Allen[1]

Received 12 August 2009; revised 10 March 2010; accepted 6 April 2010; published 20 August 2010.

[1] Three-dimensional circulation in the coastal transition zone (CTZ) off Oregon is studied using a 3 km resolution model based on the Regional Ocean Modeling System. The study period is spring and summer 2002, when extensive observations were available from the northeastern Pacific component of the Global Ocean Ecosystems Dynamics project. Our main focus is on near-surface transports, particularly in an area off Cape Blanco where an energetic coastal current is separated in the CTZ. Comparisons with available observations (velocities from midshelf moorings, surface velocities from high-frequency radars, satellite sea surface temperature maps, along-track sea surface height altimetry, and SeaSoar hydrography) show that the model reproduces qualitatively correctly the flow structure and variability in the study area. The near-surface flow behavior during 26 July to 21 August, a late-summer time period of strong, time-variable southward winds, is examined. During that period the coastal jet separates from the continental shelf around Cape Blanco (43°N). The energetic separated jet continues to flow southward in a near-coastal region between 42.2°N and 43°N. It subsequently turns around 42°N to flow westward offshore past 127°W. Relatively vigorous up- and downwelling is found concentrated in the region of the separated jet. Frontogenesis secondary circulation, nonlinear effects of the relative vorticity on the ageostrophic Ekman transport, and submesoscale instabilities contribute to the vertical circulation within the jet. Vertical velocities are found to reach 50 m $d^{-1}$ in the offshore part of the jet and 100 m $d^{-1}$ in the near-coastal part, where the jet is aligned with the wind direction.

**Citation:** Koch, A. O., A. L. Kurapov, and J. S. Allen (2010), Near-surface dynamics of a separated jet in the coastal transition zone off Oregon, *J. Geophys. Res.*, *115*, C08020, doi:10.1029/2009JC005704.

## 1. Introduction

[2] The coastal transition zone (CTZ) is a region of open ocean adjacent to the continental shelf where the dynamics is affected by shelf processes. During periods of summer upwelling off the U.S. West Coast, narrow filaments of cold water are separated from the shelf to the CTZ [*Brink and Cowles*, 1991]. For instance, off Oregon, a distinctive offshore feature in late summer is a coastal jet separated near Cape Blanco (42.8°N) [*Barth et al.*, 2000]. This jet may reach a speed of 0.8 m $s^{-1}$ at the surface [*Strub et al.*, 1991] and carry cold and nutrient-rich coastal waters as far as 200 km offshore, enhancing dynamic and biological variability in the CTZ. This prominent feature is clearly seen in satellite sea surface temperature (SST) imagery (Figure 1).

[3] The separated coastal jet is associated with various dynamical processes: frontogenesis, nonlinear jet-wind interaction, and disturbances and instabilities of different nature and scale. The objective of the present study is to investigate the near-surface structure and dynamics of the coastal upwelling jet separated off the Oregon coast by means of numerical simulations and dynamical analysis.

[4] Despite a number of studies that discuss possible mechanisms for coastal current separation off Cape Blanco, to this day there is not a settled opinion on the dominant dynamical processes. Contributing factors may include interactions with topography [*Castelao and Barth*, 2007], enhanced wind stress south of Cape Blanco [*Samelson et al.*, 2002], interactions of the coastal current with the southward undercurrent [*Barth et al.*, 2000], and alongshore pressure gradients set up during periods of relaxation from upwelling [*Gan and Allen*, 2002].

[5] Shelf processes are relatively better studied than those in the CTZ, owing in large part to the success of recent coordinated observational and modeling programs, e.g., Coastal Ocean Advances in Shelf Transport (see *Barth and Wheeler* [2005] and other papers in that special issue). Advances in satellite oceanography have influenced progress in understanding near-surface transports in the CTZ. However, observations of the 3-D structure of jets, eddies, and filaments in the CTZ have been limited. One of the most coordinated efforts in that regard was the CTZ program of 1986–1987 (see *Brink and Cowles* [1991] and other papers

[1]College of Oceanic and Atmospheric Sciences, Oregon State University, Corvallis, Oregon, USA.


0148-0227/10/2009JC005704

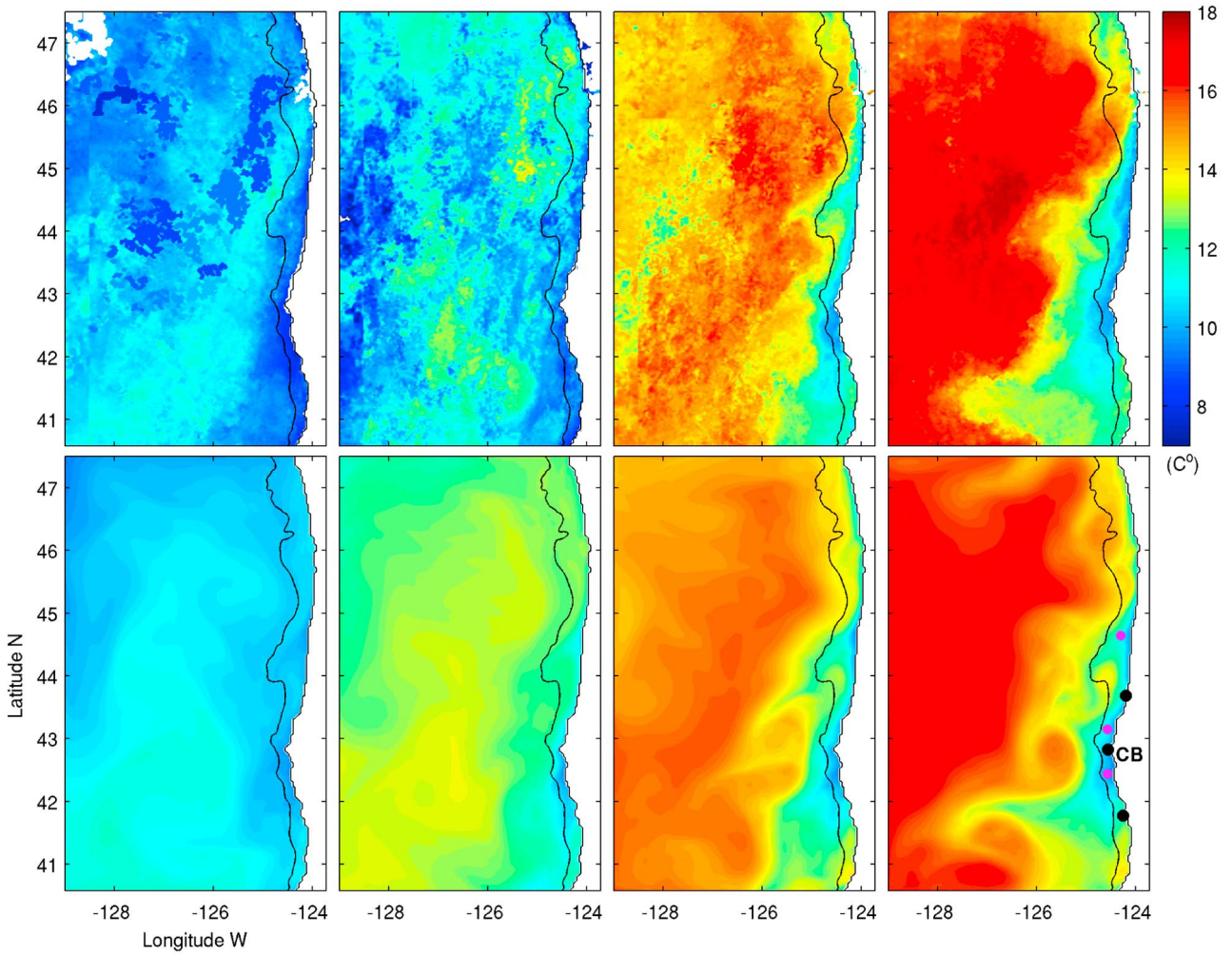


**Figure 1.** (top) Monthly SST composites from Geostationary Operational Environment Satellite (GOES) and (bottom) monthly averaged SST from ROMS for (left to right) May–August. Coastal HF-radar locations are shown in the bottom right panel by blue circles, and midshelf moorings by magenta circles; CB, Cape Blanco. The black line shows the 200 m isobath.

in that special issue). *Kadko et al.* [1991] and *Washburn et al.* [1991] reported significant vertical transport of upwelled water within the jets as they propagate offshore. *Washburn et al.* [1991] analyzed phytoplankton data to track coastal water that moves offshore and found that the near-surface water can subduct to a depth of 100 m within the jet core. The associated estimated vertical speed reached 6–10 m $d^{-1}$. *Dewey et al.* [1991] explored the structure and dynamics of a coastal upwelling jet separated off Point Arena, California, based on observations made over a 2 week period during sustained southward wind. They found asymmetry in the cross-jet relative vorticity and evidence for downwelling and upwelling within the jet. The estimated maximum vertical velocities reached 40 m $d^{-1}$ and were thought to be associated with the observed asymmetry in the relative vorticity field.

[6] Numerical modeling studies focused on California-Oregon shelf flows [e.g., *Gan and Allen*, 2002; *Castelao and Barth*, 2007] do not always correctly reproduce the westward extent of separation in the CTZ, potentially because of a limited domain size, idealized boundary conditions, and wind stress. However, jets extending off main topographic coastal features were obtained in multiyear simulations using a regional-scale 5 km resolution model of the U.S. West Coast run with seasonally varying atmospheric forcing [*Marchesiello et al.*, 2003]. *Springer et al.* [2009] developed a 3 km resolution model based on the Regional Ocean Modeling System (ROMS) with realistic atmospheric forcing and boundary conditions provided by the Naval Coastal Ocean Model California Current System (NCOM-CCS) [*Shulman et al.*, 2004]. The 3 km ROMS model reproduces coastal jet separation off Cape Blanco qualitatively correctly. That study focused more on shelf processes and did not examine dynamical processes in the CTZ, in particular, the jet structure. In this paper, we use a similar model configuration to simulate flows from summer 2002, when extensive observations from the Global Ocean Ecosystems Dynamics in the northeastern Pacific (GLOBEC-NEP) field program [*Strub et al.*, 2002] are available. We use those data to evaluate model performance. Then, we analyze

the structure of the jet separated off Cape Blanco with an emphasis on near-surface behavior, particularly under strong wind conditions.

## 2. Model

[7] Our model is based on ROMS, which is a free-surface, terrain-following, primitive equation ocean model widely used by the scientific community for various applications [e.g., *Haidvogel et al.*, 2000; *Marchesiello et al.*, 2003; *Di Lorenzo*, 2003]. Algorithms that comprise a ROMS computational kernel are described in detail by *Shchepetkin and McWilliams* [2003, 2005].

[8] The model computational domain, shown in Figure 1, extends from 40.5°N to 47.5°N in the meridional direction and from the coast, near 124°W, offshore to 129°W. The grid has approximately 3 km horizontal resolution and 40 terrain-following layers in the vertical with a relatively better resolution near surface and bottom. Bottom topography is composed by merging two sets: a high-resolution (12″) NOAA-National Geophysical Data Center bathymetry of the U.S. West Coast, representing features on the shelf and continental slope, and a lower-resolution (5′) ETOPO5 product [*National Geophysical Data Center*, 1988]. A minimum depth of 10 m is set along the coastline.

[9] The study period is from 1 April to 31 August 2002. Initial and boundary conditions are obtained from the 9 km horizontal resolution NCOM-CCS model [*Shulman et al.*, 2004] that spans between (134.5°W, 116°W) and (30°N, 48.5°N). The NCOM-CCS solution was constrained by assimilation of sea surface height (SSH) and SST using a nudging approach [*Shulman et al.*, 2004, 2007]. At the open boundaries of our model, the free-surface elevation, barotropic and baroclinic velocities, water temperature, and salinity are provided daily. Radiation conditions in combination with a relaxation nudging term are applied for baroclinic velocities and for temperature and salinity at open boundaries [*Marchesiello et al.*, 2001]. Flather conditions [*Flather*, 1976] are utilized for the normal barotropic velocities, and Chapman conditions for the free surface [*Chapman*, 1985].

[10] To force our model, we calculate surface wind stress from the same time- and space-dependent surface wind velocity fields that were originally used to force NCOM-CCS, provided from the Coupled Ocean/Atmosphere Mesoscale Prediction System (COAMPS) [*Hodur*, 1997] with 9 km horizontal and daily temporal resolution. Other atmospheric variables (air temperature, pressure, relative humidity, precipitation, and solar short-wave radiation), used to compute atmospheric fluxes based on bulk flux parameterizations [*Fairall et al.*, 2003], are obtained from the National Centers for Environmental Prediction (NCEP) reanalysis [*Kalnay et al.*, 1996] and are provided as monthly fields, describing seasonal variability. Figure 2 shows time series of the wind stress at two midshelf locations within the model domain, near Newport (44.6°N) and the Rogue River (42.4°N), projected onto their respective major principal axes, which are approximately aligned with the coast. During spring and summer the wind stress over the Oregon shelf is predominantly southward with rare and short events of northward, downwelling favorable winds. The wind stress is substantially larger south of Cape Blanco [*Samelson et al.*, 2002].

[11] The effects of vertical turbulence are calculated using *Mellor and Yamada*'s [1982] 2.5-level turbulence closure scheme, modified by *Galperin et al.* [1988]. Horizontal turbulence is parameterized using a harmonic term with eddy diffusivity and viscosity coefficients of 10 $m^2 s^{-1}$. To minimize the effects of reflection at the boundaries, a sponge layer is introduced in an area of width 120 km along the open boundaries, in which horizontal dissipation is gradually increased to 30 $m^2 s^{-1}$ toward the edges of the domain.

## 3. Model-Data Comparisons

### 3.1. Sea Surface Temperature

[12] A comparison of the model monthly averaged SST with 5 km horizontal resolution monthly SST composites from the GOES [*Maturi et al.*, 2008] shows that the model simulates the seasonal development of the surface temperature field qualitatively correctly (Figure 1). In the plots of the satellite measurements for June and July, patches of cooler temperature can be associated with clouds. The extent of the temperature front off Cape Blanco, particularly apparent in July and August, is similar in the model and in the satellite imagery. The features of the temperature front in the monthly means are sharper in the model plots than in the satellite plots. We hypothesize that small-scale horizontal eddy fluxes, unresolved in our model, could contribute to smearing the monthly mean observed fronts and to increased temporal variability of the jet position.

### 3.2. Acoustic Doppler Current Profiler Velocities

[13] Continuous time series of acoustic Doppler current profiler velocities were measured in 2002 at three midshelf moorings: NH10, 44.6°N, in water depth $H$ = 81 m [*Kosro*, 2003]; Coos Bay, 43.2°N, $H$ = 100 m (B. M. Hickey, personal communications); and Rogue River, 42.4°N, $H$ = 76 m [*Ramp and Bahr*, 2008]. Mooring locations are shown in Figure 1. Figure 2 shows time series of 40 h low-pass filtered depth-averaged velocities at the mooring locations, model and observations, projected onto their respective major principal axes that deviate slightly from the meridional direction. At each mooring, the model-data correlation coefficient is high (>0.68), and the root-mean-square error is low (<0.14 m $s^{-1}$). At the Rogue River mooring, south of Cape Blanco, the observations show increased variability on the temporal scale of several days that is not well described by the model (see Figure 2e). This variability correlates with that in the wind stress (Figure 2b). The reason for this strong response to the wind in this frequency band is not entirely understood. However, we speculate that part of that response may be because of remote forcing south of our domain that is not totally represented by the southern boundary conditions. Figure 3 shows time-averaged means and variance ellipses for the depth-averaged currents at the mooring locations. Both the data and the model reveal larger current variability in the alongshore direction. The magnitude and direction of the mean current and the variance are very similar in data and model. Curiously, the mean current at the Rogue River site inside the separation zone south of Cape Blanco is close

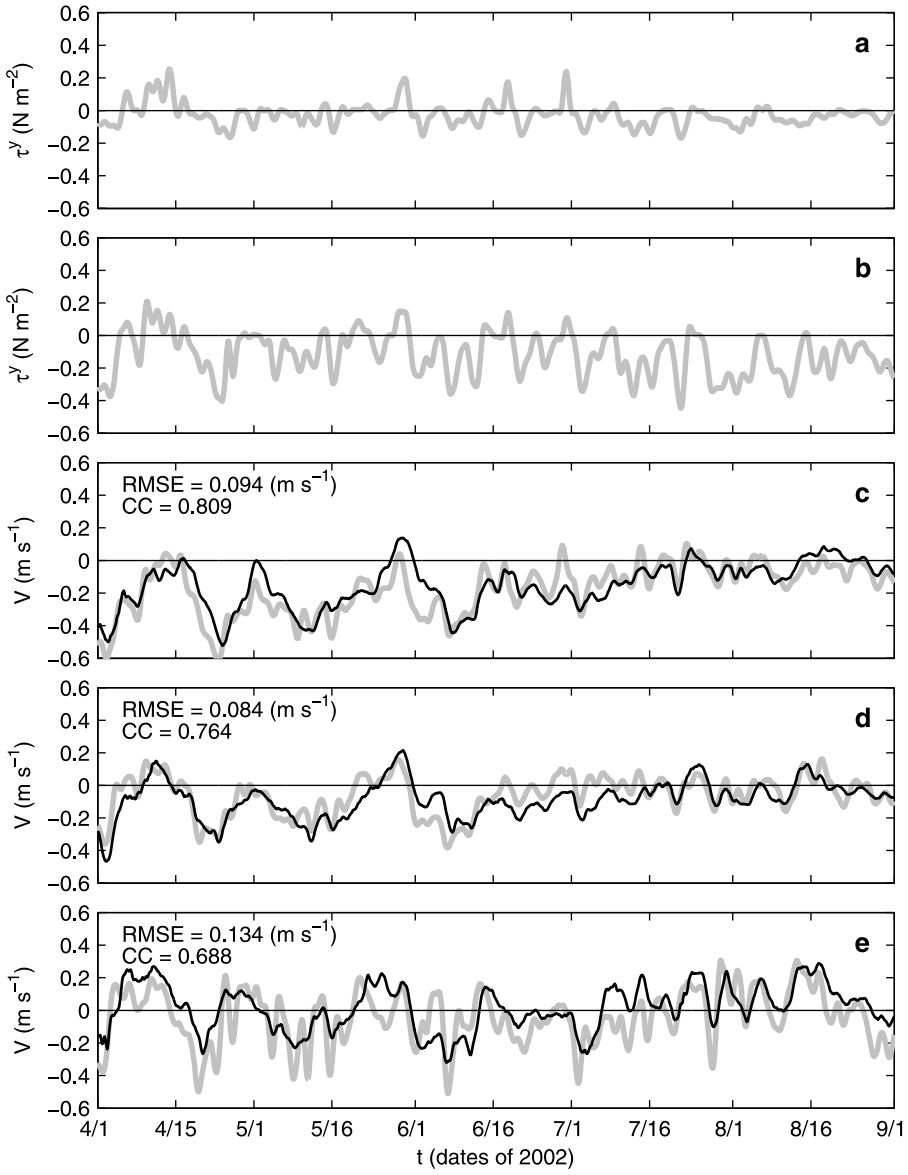


**Figure 2.** Alongshore COAMPS wind stress $\tau^y$ at the (a) NH10 (44.6°N) and (b) Rogue River (42.4°N) moorings, and depth-averaged alongshore current $V$ at (c) NH10 (44.6°N), (d) Coos Bay (43.2°N), and (e) Rogue River (42.4°N) mooring observations (shaded lines) and model (black lines). Variables are presented along respective major principal axes. Root mean square error (RMSE) and correlation coefficients (CC) for data and model are shown.

to zero, despite large and predominantly southward wind stress at that location.

[14] Time-averaged statistics of the measured currents from the three moorings are compared with corresponding model currents as a function of depth in Figure 4. Fairly good agreement of the observed and modeled mean values and standard deviations for both the larger alongshore $v$ and smaller cross-shore $u$ components is found at NH10 and Coos Bay. At Rogue River, the signs of the observed and modeled mean $v$ differ below 25 m, but both are relatively small. The standard deviations at Rogue River are similar in magnitude to those at NH10 and Coos Bay, with observed values slightly larger. At all of the moorings, the correlations of the observed and modeled alongshore velocity $v$ are reasonably high while those of the cross-shore velocity $u$ are considerably lower. Likewise, the normalized root-mean-square errors are substantially lower for $v$ than for $u$. The greater success in modeling the fluctuations in the larger alongshore currents $v$ compared with the smaller cross-shore currents $u$ is consistent with previous model results for midshelf currents off Oregon [e.g., *Springer et al.*, 2009].

### 3.3. HF-Radar Currents

[15] To assess the accuracy of model surface currents in the area around Cape Blanco, we compare the model and maps derived from long-range HF radars [*Paduan et al.*,

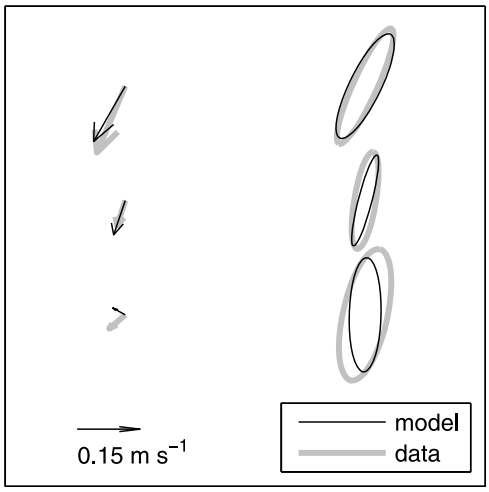


**Figure 3.** Mean and variance ellipses for depth-averaged currents at the mooring locations (top) NH10, (middle) Coos Bay, and (bottom) Rogue River for observations (gray) and model (black) over the calculation interval (see Figure 2).

2004; *Kosro*, 2005]. HF radar locations are shown in Figure 1. The radial velocity components with 6 km along-beam resolution were low-pass filtered, recomputed into zonal and meridional components, daily averaged, and mapped on a 6 km regular grid by P.M. Kosro (OSU). Figure 5 shows observed and model monthly averaged surface current, speed, and the RMS speed of deviations from the mean, defined as

$$U_{\mathrm{RMS}} = \left[\overline{(u-\overline{u})^2 + (v-\overline{v})^2}\right]^{\frac{1}{2}}, \qquad (1)$$

where the overbar denotes a time average.

[16] The model and observed current patterns are qualitatively comparable. In May the surface jet is already separated from the Cape and flows southward. By July, the observed currents form two jets, one south and one north of Cape Blanco. A similar structure is seen in the model, although it appears earlier in June. The observed jets are wider and less energetic than modeled, which may come partly from the smoothing effect of the mapping procedure performed on the radial data and/or from small-scale eddy variability unresolved in the model. By August, when the model jet turns westward at 42°N, the data show a similar westward orientation of the flow, although the observed monthly mean is diffused over a larger area. The magnitude of the monthly averaged model current within the jets is similar to observed magnitudes in May–June (0.3–0.5 m s$^{-1}$) and is 30–40% higher in the model (0.6–0.7 m s$^{-1}$) than in the observations (0.2–0.5 m s$^{-1}$) in July–August. The variability of the current, shown by $U_{\mathrm{RMS}}$ (Figure 5), is of the same order (0.1–0.25 m s$^{-1}$) in the observations and the model for May–July, with increased variability found over the shelf and in the CTZ jets. Although variability in the HF-radar data in August (0.1–0.2 m s$^{-1}$) is lower than in the model (0.02–0.3 m s$^{-1}$), it is distributed more evenly over the area. This, together with the fact that the observed mean currents are more spatially uniform than the modeled currents, suggests that the position of the observed separated jet fluctuates over the domain more than that of the modeled jet. Again, we speculate that eddy variability on scales <10 km, not represented in our model, contributes to jet instability and variability.

[17] Despite the fact that the jet is not seen clearly in monthly averaged observed fields in August, it may be readily identified in daily plots (Figure 6). The dates in Figure 6 are chosen so that satellite SSH observations are available along the track that passes through the area (shown as the white line; see discussion in section 3.4). The model and observed jets in the daily plots (Figure 6) are found to have comparable speeds (0.6–0.8 m s$^{-1}$) and across-jet spatial scales (10–30 km).

### 3.4. Sea Surface Height

[18] In summer 2002, the Archiving, Validation, and Interpretation of Satellite Oceanographic data (AVISO, http://www.aviso.oceanobs.com) satellite SSH altimetry (sea level anomaly) is available along the orbits of the TOPEX/POSEIDON satellite with 10 day periodicity [*Fu et al.*, 1994]. Six tracks cross our model domain area. Here we show comparison with the data from track 206, which passes through the area covered by the HF radar (see Figure 6). For this analysis, along-track means are removed from both model and observational lines. The variability in SSH is of similar magnitude and horizontal scale in both the satellite data and the model and can be associated with jets and eddies in the CTZ. The SSH gradient is proportional to the surface geostrophic current normal to the track. Using the satellite data, the estimated geostrophic current in the jets can be as large as 0.6–0.8 m s$^{-1}$. However, the location and intensity of individual jets and eddies in the along-track data and model do not necessarily coincide. It is possible that assimilation of SSH data in a model of this class can improve the representation of the time-dependent eddy-dominated flows in the CTZ.

### 3.5. Density

[19] In the beginning of August 2002, vertical cross-shore sections of potential density $\sigma_\theta$ were measured as part of a SeaSoar survey [*Barth et al.*, 2005; see also *O'Malley et al.*, http://damp.coas.oregonstate.edu/globec/nep/seasoar]. The comparisons of three cross-shore density sections measured along 41.9°N, 43.5°N, and 44.25°N in the beginning of August with sections sampled at the same times and locations as the model results are presented in Figure 7. There is a qualitative and quantitative agreement between data and model in the two sections north of Cape Blanco (Figures 7a–7d), especially in the shape, slope, and spacing of the isopycnals that provide information on properties of the upwelling density front, and the associated normal geostrophic flow. The model-data agreement in the southernmost section is not as close. In particular, the eddy shown by the uplift of isopycnals near 125.3°W (Figure 7e) is only weakly represented in the model section (Figure 7f). This behavior reflects the difficulty, found also in section 3.4 in connection with model-data SSH comparisons, of deterministically modeling

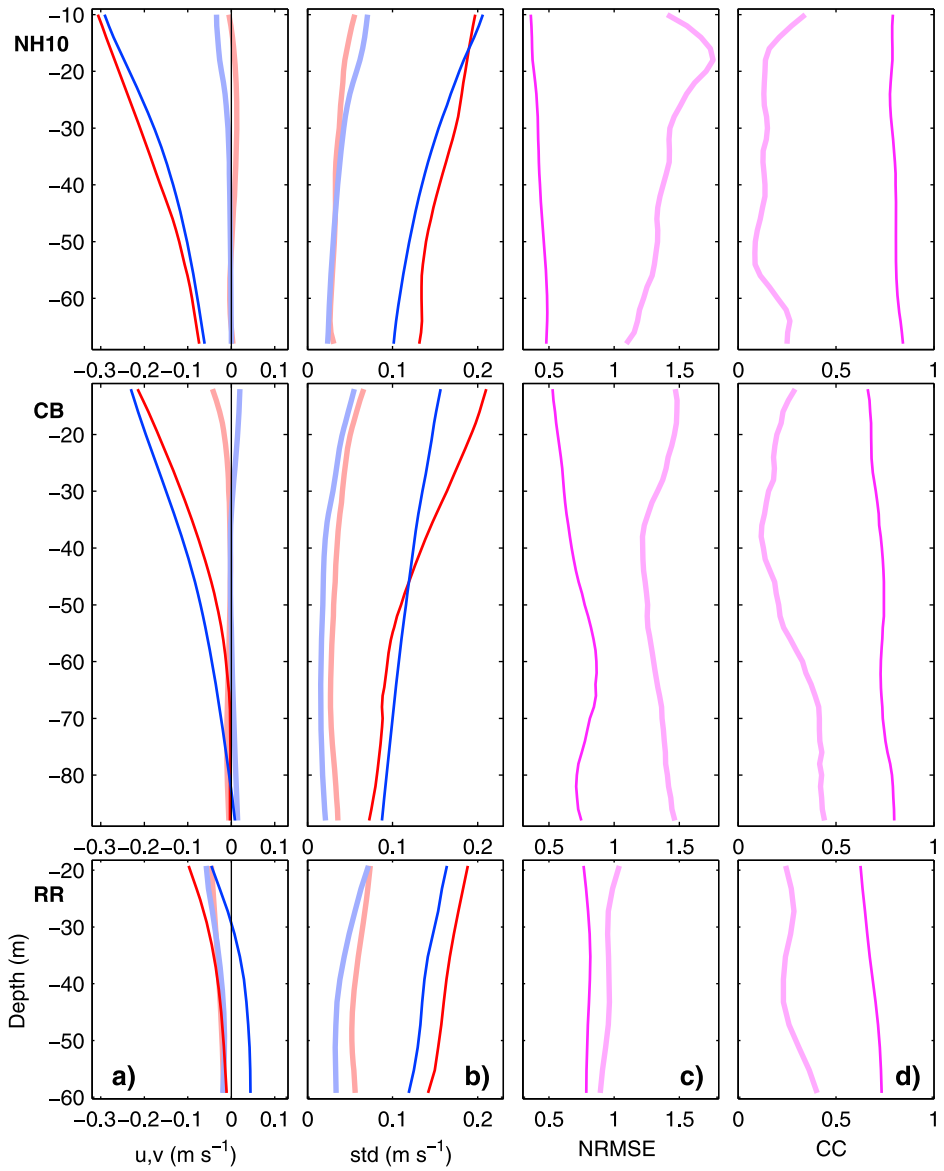


**Figure 4.** Vertical profiles of time-averaged statistics for cross-shore $u$ (pale colors, thick lines) and alongshore $v$ (bright colors, thin lines) components of velocity projected on respective principal axes of the depth-averaged velocities: (a) means, (b) standard deviations (std), (c) normalized root-mean-square error (NRMSE), defined as NRMSE = $[\overline{(u_{obs} - u_{mod})^2}/\overline{u_{obs}^2}]^{1/2}$, where the overbar denotes a time average, and (d) correlation coefficients (CC). In Figures 4a and 4b, red lines denote observations blue lines denote model results. Data are taken from midshelf moorings: (top) NH10, (middle) Coos Bay, and (bottom) Rogue River.

the individual filaments and eddies in the energetic separated flow region offshore south of Cape Blanco.

## 4. Dynamical Analyses of Jet Structure

### 4.1. Mean Near-Surface Circulation

[20] To explore the mean near-surface circulation in the CTZ off Oregon, we choose a late summer 27 day time interval from 26 July to 21 August when the wind over the study area is generally upwelling-favorable, but varies in time on a typical several-day time scale (Figure 8) and the separated jet is well developed and extends offshore as far as 200 km (Figure 9). The region of relatively large horizontal gradient of the time-mean surface density field, along with the SSH field, shows the upwelling front location (Figure 9, left). The coastal upwelling jet is rather discontinuous along the front and breaks into a few separation zones. The separated jet intensifies and reaches maximum values of 0.6–0.7 m s$^{-1}$ south of Cape Blanco (Figure 9, right). The maximum jet variability is found within these separation zones. North of the Heceta Bank complex, around 45°N, the separated jet has approximately equal strengths in its along- and normal-to-coast components. In contrast, offshore in the separation zone south of Cape Blanco, the jet is noticeably

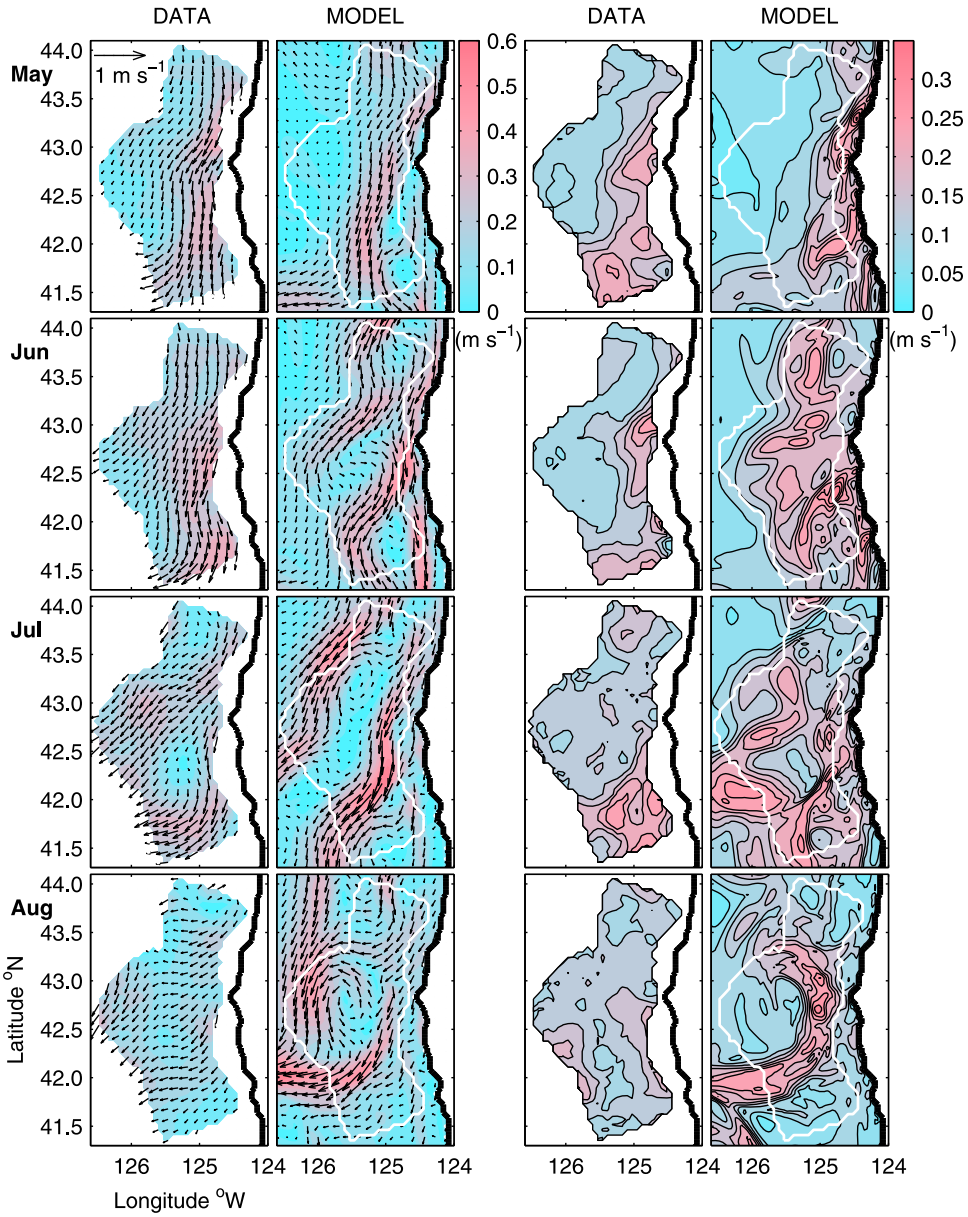


**Figure 5.** Surface current statistics from HF radar and model for May–August (top to bottom): (left) monthly averaged current vectors **u** and speed |**u**| in color and (right) RMS speed deviations from the mean $U_{\mathrm{RMS}} = \overline{[(u-\overline{u})^2 + (v-\overline{v})^2]}^{1/2}$, where the overbar denotes a time average. Color contour intervals for $U_{\mathrm{RMS}}$ are 0.03 m s$^{-1}$. The white contour on the model fields shows the area of the corresponding data coverage.

stronger than its upstream along-coast link, whose strength may be weakened by the cyclonic mesoscale eddy, located west of the jet and centered near 43°N,125.7°W, that is stationary through the averaging interval.

[21] Horizontal fields of the mean and standard deviation of the vertical velocity at 25 m depth over this time period (Figure 10) show interesting behavior. In particular, the spatial pattern of the standard deviations of $w$, which can reach magnitudes typically two times greater (around 20 m d$^{-1}$) than the magnitudes of the mean values (around 10 m d$^{-1}$) show relatively large values strongly concentrated in the region of the separated jet. That region extends along the jet from a location within about 60 km of the coast near Cape Blanco (43°N), where the separating jet is directed southward, offshore to about 127°W, where the jet is flowing westward. The magnitude of the mean values of $w$ (Figure 10) are appreciable in a similar spatial region, but with greater values in the near-coastal location between 42.2°N and 43°N, where the jet flows southward. The behavior in that location is characterized by concentrated mean upwelling velocities offshore in the jet, with downwelling velocities immediately inshore.

[22] The horizontal spatial structure of the mean and standard deviation of the vertical velocity at 25 m depth in

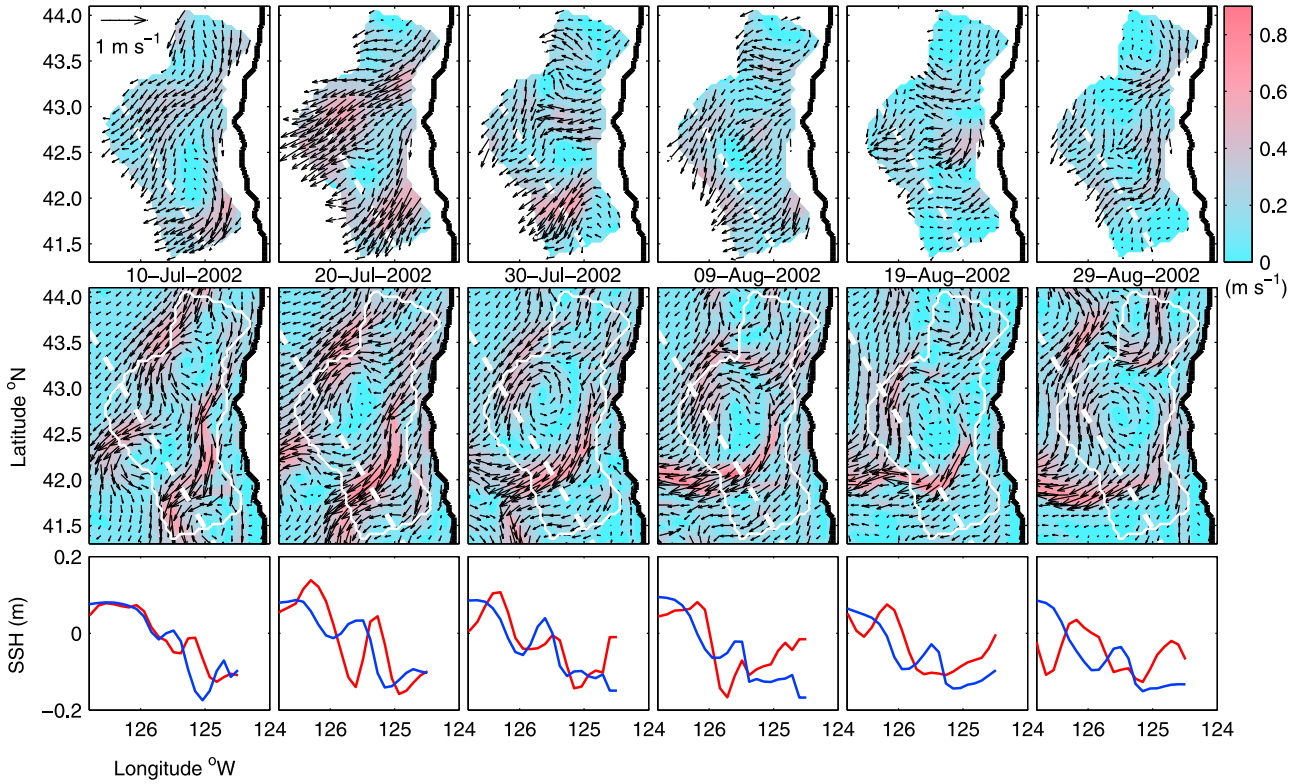


**Figure 6.** Instantaneous fields of surface current vectors **u** and speed |**u**| (color) for (top) HF radar and (middle) model in July–August in the area near Cape Blanco, and observed satellite SSH (from track 206) (red) and model SSH sampled at the same location (blue) shown at bottom. The SSH has the mean taken out. The location of track 206 is denoted by a white dashed line.

Figure 10 is remarkable. In particular, it reflects the presence of energetic near-surface ageostrophic processes that are relatively localized in the vicinity of the separated coastal jet off Cape Blanco. It also provides motivation for the analyses that follow of the time-dependent dynamics that leads to the large variability in near-surface vertical velocities in this region.

### 4.2. Lagrangian Analysis of Surface Flows

[23] To get an idea of the general character of Lagrangian flows in the CTZ during the chosen late-summer time period, we release 65 model surface particles simultaneously at 0000 (UTC, hereinafter) 1 August along the 81 m isobath (the depth of mooring NH10) every 10 km in the meridional direction between latitudes 41°N and 47°N. Model trajectories are obtained by integration of surface velocities, saved every 4 h, using a fourth-order Runge-Kutta method. The particles, advected by the surface current, begin to group in offshore directed filaments over the initial period 1–10 August (Figure 11). The speed of the particles entrained in filaments can be several times greater than the speed associated with the offshore Ekman transport. For the trajectories over 1–20 August (Figure 11), we can see two major compact jets, originating over the shelf near the Heceta Bank complex (44°N) and near Cape Blanco (43°N), respectively. The pattern of surface trajectories over the Oregon CTZ (Figure 11) is qualitatively consistent with the shape of the observed SST front in August (Figure 1).

### 4.3. Surface Strain Rate Field

[24] Although the Lagrangian tracking described in section 4.2 is a powerful visualization tool, it is limited to areas where particles are seeded at an initial time or found later. To quantify the rate of relative surface particle separation over the entire domain, the surface strain rate tensor can be computed:

$$\begin{bmatrix} \varepsilon_{xx} & \varepsilon_{xy} \\ \varepsilon_{yx} & \varepsilon_{yy} \end{bmatrix} = \begin{bmatrix} \dfrac{\partial u}{\partial x} & \dfrac{1}{2}\left(\dfrac{\partial u}{\partial y} + \dfrac{\partial v}{\partial x}\right) \\ \dfrac{1}{2}\left(\dfrac{\partial u}{\partial y} + \dfrac{\partial v}{\partial x}\right) & \dfrac{\partial v}{\partial y} \end{bmatrix}, \tag{2}$$

where $(x, y)$ are local Cartesian coordinates [e.g., *Batchelor*, 1967, section 2.3]. The diagonal elements of the matrix, $\varepsilon_{xx}$ and $\varepsilon_{yy}$, represent the normal strain rate, and the nondiagonal elements, $\varepsilon_{yx} = \varepsilon_{xy}$, represent the shear strain rate. At each location, the strain rate tensor can be rotated to principal axes, in which the shear component is zero and the normal components $\varepsilon_1$ and $\varepsilon_2$ are

$$\varepsilon_{1,2} = \overbrace{\frac{1}{2}(\varepsilon_{xx} + \varepsilon_{yy})}^{\text{divergence term}} \pm \overbrace{\left[\frac{1}{4}(\varepsilon_{xx} - \varepsilon_{yy})^2 + \varepsilon_{xy}^2\right]^{\frac{1}{2}}}^{\text{deformation term}}. \tag{3}$$

The first term on the right-hand side of (3) is the divergent component. It provides an estimate of the relative particle

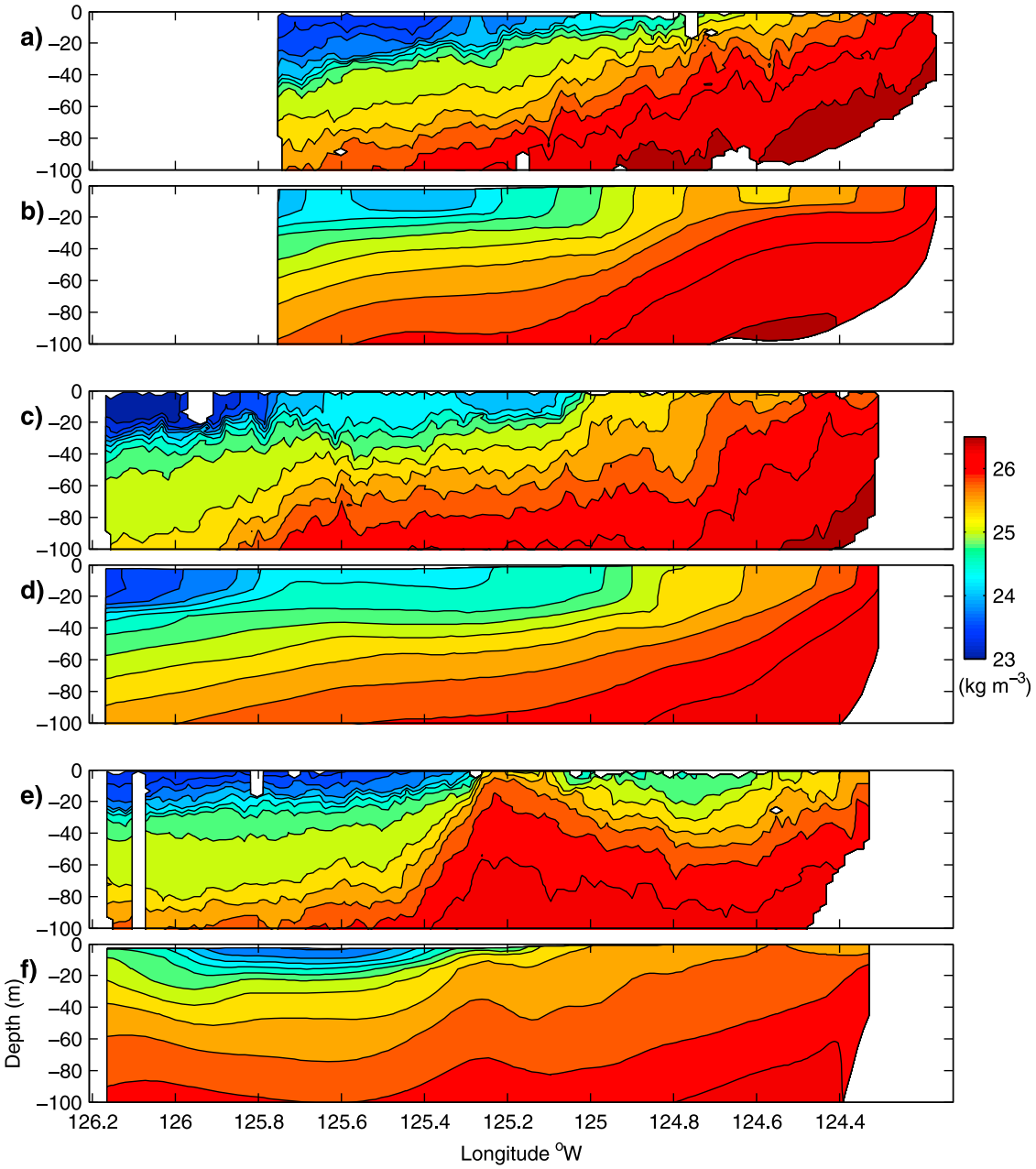


**Figure 7.** (a, c, e) Cross-shore sections of potential density $\sigma_\theta$ measured during a SeaSoar survey and (b, d, f) model fields sampled at the same times and locations as the observations, along 44.25°N during 2 August (Figures 7a and 7b), 43.5°N during 3–4 August (Figures 7c and 7d), and 41.9°N during 6–7 August (Figures 7e and 7f). Color contour intervals are 0.25 kg m$^{-3}$.

separation rate owing to the relative change of the surface area. The second, deformation component quantifies the particle separation rate owing to the change in the shape of a small surface domain, without changes of its area. We note, relevant to the calculation of the divergence term, that model surface velocities correspond to horizontal velocity components at the uppermost model grid points located vertically one half a grid cell below the surface.

[25] Figure 12 shows the two terms in the principal surface strain rate field (3), averaged over the 27 day period 26 July to 21 August. In these averaged maps, the deformation part of the principal strain rate is dominant. Note that there is divergence in the surface current near the coast associated with surface Ekman transport, although in the monthly averaged plot its magnitude is smaller than that of the deformation part of the strain rate. In the following, we examine the flow during the wind event around 1 August. On this date, offshore between 125°W and 127°W, an energetic separated jet was directed westward approximately along 42°N (Figure 13, right). The wind stress in the area of the jet is strong (−0.35 N m$^{-2}$; Figure 8) and is directed southward, nearly perpendicular to the jet direction (Figure 13, left). Velocities within the jet reach 0.9 m s$^{-1}$. During this event, the divergence term of the principal strain rate

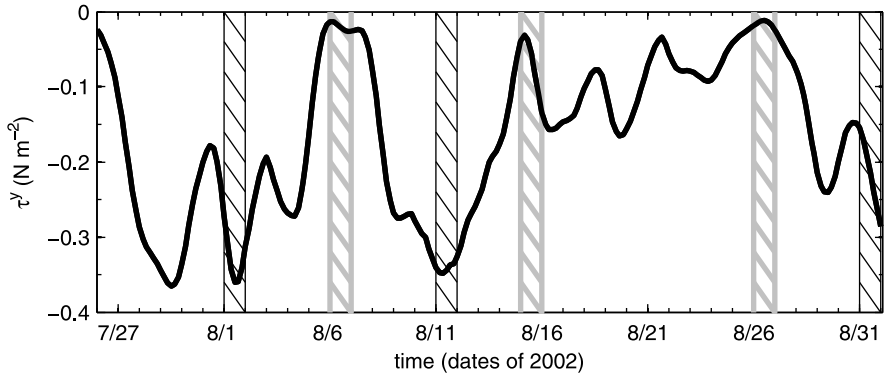


**Figure 8.** Time series of the north-south component of the wind stress $\tau^y$, averaged over the across-jet section along 126°W between 41.65°N and 42.4°N (see Figure 13), from 26 July to 31 August 2002. Black bars denote strong wind events, and shaded bars denote weak wind events.

becomes comparable in magnitude to the deformation term, particularly along the paths of the CTZ jets (Figures 12c and 12d). Both terms are increased in magnitude compared to the 27 day averages (note that color bar limits for Figures 12a–12d are different). Since the divergence of the surface horizontal flow is attributed entirely to its ageostrophic component, i.e., $\nabla_h \cdot \mathbf{u} = \partial u_a/\partial x + \partial v_a/\partial y$ (section 4.4), this analysis provides an additional indication of the important role of time-dependent ageostrophic processes in the near-surface dynamics of the separated jet south of Cape Blanco.

### 4.4. Structure of the Separated Jet on 1 August

[26] To study further the nature of the flow that leads to the large mean and RMS near-surface vertical velocities in the region of the separated jet (Figure 10), we examine some instantaneous horizontal fields and vertical sections from 1 August, during a period of strong southward winds (Figure 8) when the offshore separated jet is well developed (Figure 13, right). The wind stress field on 1 August (Figure 13, left) shows the known spatial increase in magnitude of the wind stress south of Cape Blanco [*Samelson et al.*, 2002]. It also shows that on 1 August the stress vectors have a predominantly north-south direction in the region of the separated jet (41.5°N–43°N, 124.5°W–127°W). We look first at the vertical jet structure along two sections: one near-coastal, east-west section along 42.63°N and one offshore, north-south section along 126°W (locations shown in Figure 13). Instantaneous values of potential density $\sigma_\theta$, the

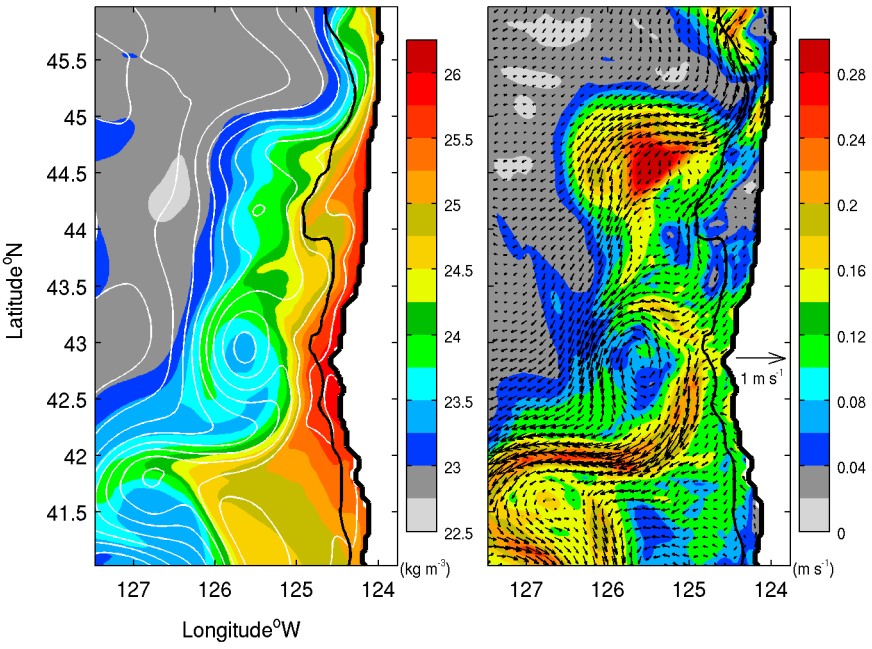


**Figure 9.** (left) Surface potential density $\sigma_\theta$ in color and SSH in white contours and (right) surface current vectors **u** and their standard deviations in color, averaged over 26 July to 21 August. Contour intervals for SSH are 0.03 m. The solid black line shows the 200 m isobath.

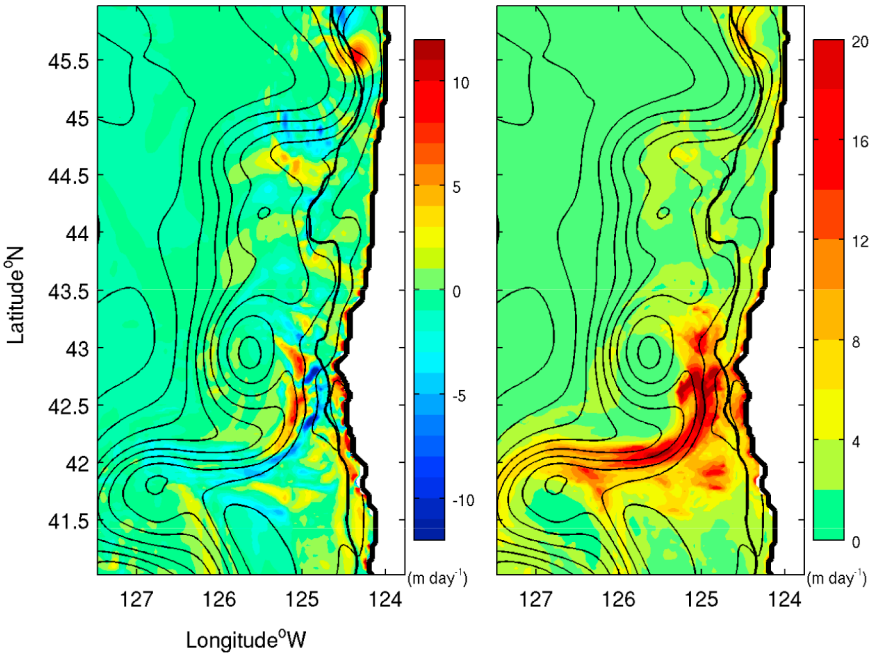


**Figure 10.** (left) Mean vertical velocity $w$ at 25 m depth and (right) its standard deviation in color and SSH in black contours, averaged over 26 July to 21 August. Contour intervals for SSH are 0.03 m. The solid black line shows the 200 m isobath.

respective geostrophic along-jet velocity components $v_g = (1/f\rho_0)(\partial p/\partial x)$ and $u_g = -(1/f\rho_0)(\partial p/\partial y)$, and the ageostrophic velocity components $v_a = v - v_g$ and $u_a = u - u_g$, where $f$ is the Coriolis parameter, $\rho_0$ is the reference density, and $p$ is the pressure, are shown in Figure 14.

[27] At the location of the near-coastal, east-west section, the coastal jet has separated offshore of the continental shelf but is still flowing southward in the direction of the wind stress (Figure 13). The dominant along-jet velocities $v$ are in geostrophic balance with a density field characterized by a strong upwelling frontal structure (Figure 14). There is some augmentation of the southward geostrophic velocities $v_g$ by an ageostrophic component $v_a$ in the jet core. The across-jet and vertical ageostrophic velocities exhibit characteristics of frontogenesis secondary circulation (FSC) [*Hoskins*, 1982; *Capet et al.*, 2008b]. That circulation is dominated by vigorous downwelling on the inshore, high-density side of the jet, concentrated in a region with small horizontal scale of about 10 km. Correspondingly vigorous upwelling occurs adjacently, on the lower density side over a similar short horizontal scale. The vertical scales of the larger down- and upwelling velocities extend to about 90 m depth. The near-surface ageostrophic velocity component $u_a$ is primarily negative and directed offshore, presumably driven by the southward wind stress in general accordance with Ekman dynamics. In the vicinity of the front, however, $u_a$ weakens considerably and reverses sign as it takes part in the vertical circulation processes. The basic characteristics of this wind-intensified FSC are in agreement with that predicted by recent theoretical and modeling studies [e.g., *Thomas and Lee*, 2005]. We note that $u_a$ appears to be larger in magnitude offshore on the negative vorticity side of the jet, which would be consistent with the nonlinear effect of the geostrophic relative vorticity $\partial v_g/\partial x$ on the Ekman dynamics [*Stern*, 1965; *Niiler*, 1969; *Thomas and Lee*, 2005], represented as

$$M_E^x = \int_{-\delta_E}^{\eta} u_a \, dz = \frac{\tau^y}{\rho_0 (f + \partial v_g/\partial x)}. \tag{4}$$

[28] At the location of the offshore north-south section, the separated jet is flowing westward (Figure 13). During this strong wind event (and during the entire averaging period of 26 July to 21 August) the separated jet advects cold dense water, upwelled near the coast, westward (Figure 13). By the thermal wind balance, the vertical shear in $u_g$ (Figure 14) is of opposite signs on the two sides of the jet. As a result, the zonal along-jet geostrophic velocity $u_g$ has an asymmetric structure in the across-jet north-south section. The negative along-jet $u_g$ velocities are strengthened in this section by a negative ageostrophic component $u_a$, which appears to be primarily wind-driven but is again relatively large locally in the jet core. The ageostrophic component $v_a$ is negative (southward) near the surface and positive at depths greater than about 20 m, with notably larger magnitudes on the northern, negative-vorticity, side of the jet. Energetic vertical circulation is present, involving upwelling concentrated in a small $O$ (10 km) horizontal-scale region on the northern, lower density side of the jet with adjacent downwelling on a similar horizontal scale on the southern, higher-density side. This vertical circulation appears to be primarily associated with along-jet submesoscale instabilities (discussed in section 4.5). We note that the structure of the vertical velocity is qualitatively similar to the conceptual picture of vertical processes in an observed CTZ jet based on the analysis of hydrographic data in the CTZ field experiment [*Dewey et al.*, 1991].

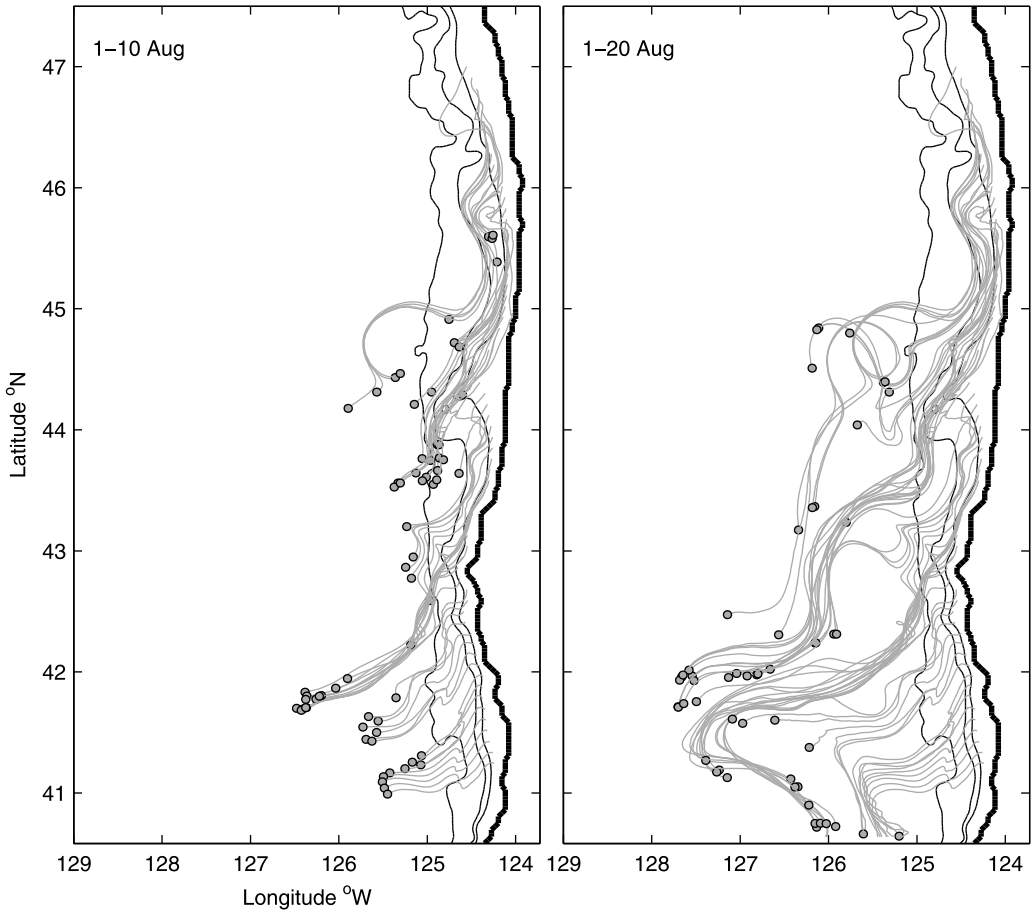


**Figure 11.** Lagrangian surface particle trajectories (gray lines) during (left) 1–10 August and (right) 1–20 August. Particles are released simultaneously on 1 August along the 81 m isobath (depth of NH10 mooring) every 10 km in the meridional direction. Circles denote particles' final locations if they are within the domain. The coastline is shown in bold, and isobaths at 100, 200, and 1000 m are shown as thin black lines.

[29] To examine other dynamical features associated with the separated jet in these two locations, we plot in Figure 15 corresponding across-jet vertical sections of buoyancy frequency $N^2 = -(g/\rho_0)(\partial\sigma_\theta/\partial z)$, turbulent vertical diffusivity coefficient $K_h$, turbulent kinetic energy (TKE), including contours of the Richardson number $Ri = N^2/S^2$, where $S^2 = (\partial u/\partial z)^2 + (\partial v/\partial z)^2$ is the sum of the squared vertical shear of the horizontal velocity components, and turbulent shear production $P = K_m S^2$, where $K_m$ is the turbulent vertical viscosity coefficient [e.g., *Wijesekera et al.*, 2003]. In both sections, large values of buoyancy frequency (Figures 15a–15e) reflect stable vertical stratification and correspond to the areas of relatively large vertical density gradients (Figures 14a–14f). Areas of unstable stratification with negative $N^2$, marked by the white stars, result, through the turbulent closure scheme, in accompanying large values of vertical diffusivity $K_h$ (Figures 15b–15f). In the coastal section, the unstable region with large $K_h$ at about 124.9°W appears to be related to the downwelling circulation at that location, but unstable conditions are found at other locations away from the frontal regions of strong vertical circulation as well. In both sections, regions of relatively large TKE are found in the surface layer on the light side of the front (Figures 15c–15g), reflecting the results of relatively large shear production $P$ (Figures 15d–15h) in those locations. In the offshore section, the region of large surface-layer TKE is considerably greater and extends farther from the jet core. An additional analysis (not shown here) shows that the enhanced shear production in that region is caused by the shear in the ageostrophic across-jet velocity component $v_a$.

[30] The sections of TKE and $K_h$ (Figure 15) show significant spatial variability that evidently has some relation to the presence of the separated jet. To examine that behavior further, we plot in Figure 16 horizontal fields from 1 August of relevant variables, including ageostrophic surface velocity vectors superposed on the relative vorticity $\zeta_g$ of the geostrophic surface currents, the maximum value in the upper 25 m of TKE, and the maximum value in the upper 25 m of the turbulent closure scheme stability function $G_h = \min(-l^2N^2/2\text{TKE}, 0.028)$, where $l$ is a turbulent length scale [e.g., *Wijesekera et al.*, 2003]. A relationship between the surface ageostrophic currents and the surface geostrophic vorticity is apparent in the horizontal fields. The direction of the surface ageostrophic velocity vectors is locally changed in areas of jet flows where the vorticity changes its sign (Figure 16, left). The across-jet sections (Figures 15c–15g) indicate that the TKE is strongly affected by the ageostrophic processes in the surface layer. The horizontal field of

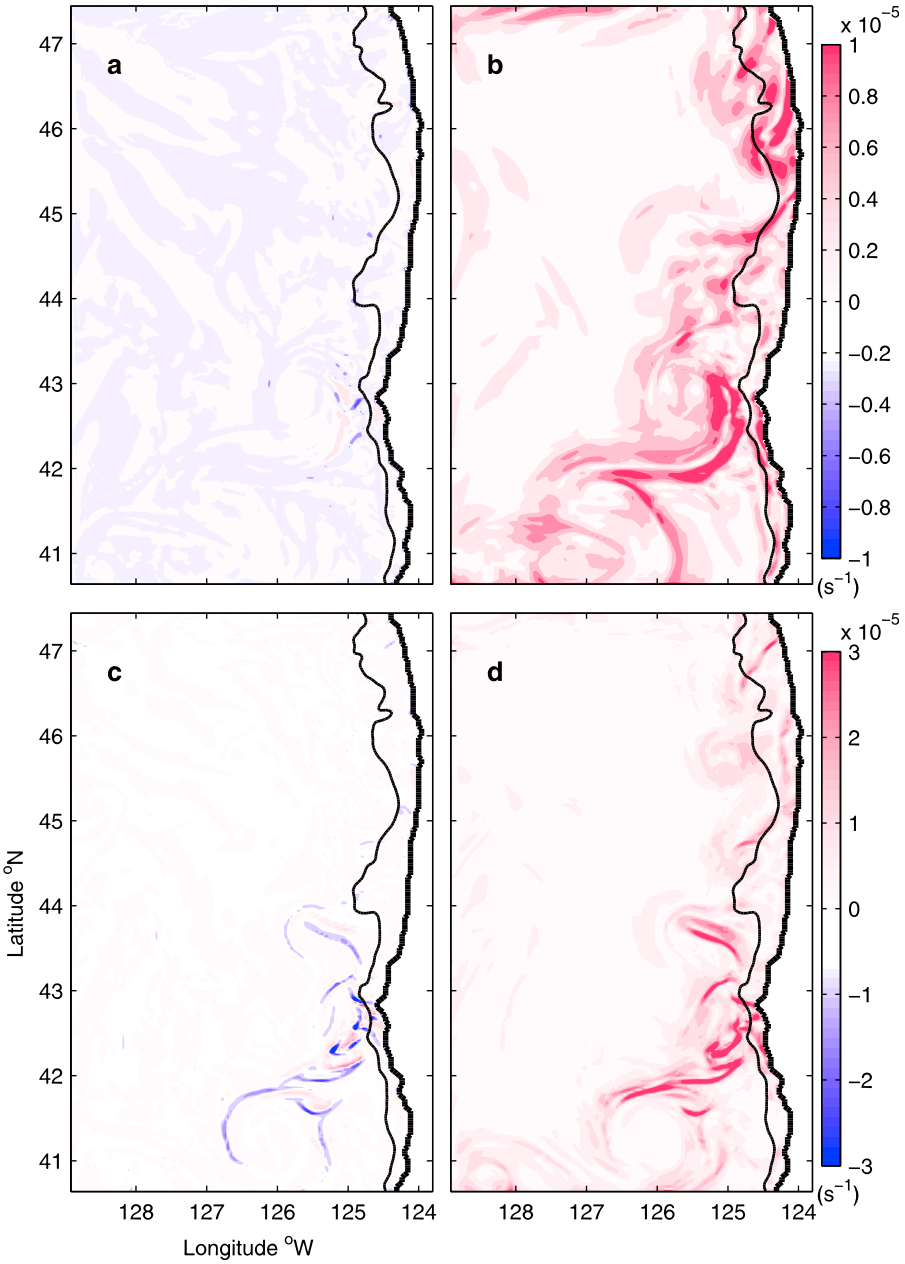


**Figure 12.** (a, c) Divergence and (b, d) deformation terms of the surface strain rate field (3) averaged over 26 July to 21 August (Figures 12a and 12b) and at 0800 1 August (Figures 12c and 12d). The solid black line shows the 200 m isobath.

the maximum value of TKE in the top 25 m (Figure 16, middle) gives an assessment of the spatial extent of that effect. Spatial variability in the near-surface TKE field has two distinguishable patterns. First, the relatively large values in the region south of Cape Blanco, with a maximum close to the shelf break around 42°N, have a spatial pattern closely related to that of the wind stress (Figure 13) and clearly represent the response of the surface-layer TKE to the increased wind stress in that region. Second, the zonally oriented deep-red patch along 42°N represents the TKE associated with the separated jet. The origin of the "jet-born" TKE pattern can be found in the area of negative vorticity north of the narrow strip of zero vorticity along the jet axis (Figure 16, left). The negative vorticity appears to affect the ageostrophic velocity, evidently contributing to an increase in its meridional component $v_a$ close to the surface. This leads to increased vertical shear in $v_a$ in the surface layer, visible in the offshore section along 126°W (Figure 14i), and a corresponding increased production of TKE (Figure 15g). The local increase in the TKE offshore just north of the jet axis consequently appears to be forced in response to increased shear in the cross-jet ageostrophic velocity. Note that the dominant spatial variability in the near-surface TKE and hence in the depth of the surface boundary layer (SBL) is found at scales smaller than the scales of the wind stress. This finding suggests that the approach to obtain estimates

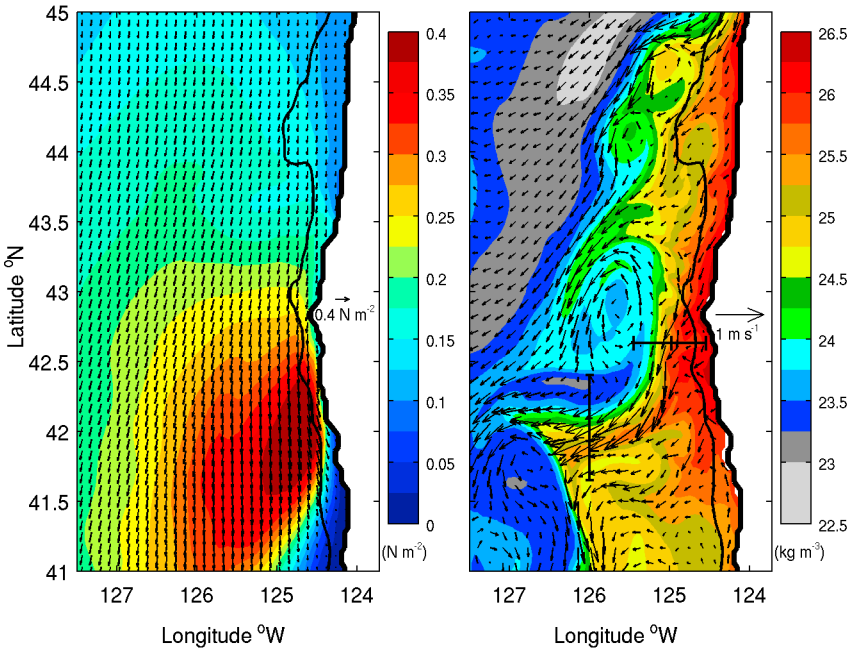


**Figure 13.** (left) Surface wind-stress magnitudes in color and directions in vectors and (right) surface potential density in color and surface velocity **u** in vectors at 0800 1 August. Cross-jet section locations along 42.63°N and 126°W, respectively, are shown (right) by straight lines, where the middle tick denotes the jet axis location. The solid black line shows the 200 m isobath.

of surface currents from the satellite information alone (SSH and wind stress), based on the assumption about the spatially uniform SBL depth [e.g., *Saraceno et al.*, 2008], can be limited in the CTZ.

[31] To assess the spatial extent of unstable stratification indicated by the vertical sections of $N^2$ and $K_h$ in Figure 15, we examine a horizontal field of the maximum of the stability function $G_h$ [e.g., *Wijesekera et al.*, 2003] in the upper 25 m from 0800, 1 August (Figure 16, right). Negative values of $G_h$ correspond to areas of stable stratification, whereas positive values correspond to areas of unstable stratification and result in accompanying large values of $K_h$. We note that there are extensive regions of positive $G_h$ in the CTZ surface layer and that most of the patches of larger horizontal scale are offshore of 126°W. In general, the patches of positive $G_h$ (Figure 16, right) can be identified with areas where the surface flow direction is not aligned with the surface isopycnals (Figure 13, right) and the advection of heavier water over light water occurs. Note that these regions are not necessarily associated with the most energetic features of the surface velocities associated with the separated coastal jet.

### 4.5. Time-Dependent Behavior in the Separated Jet

[32] To examine time-dependent behavior in the separated jet, we plot in Figure 17 horizontal fields of vertical velocities $w$ at 25 m depth, the relative vorticity of the surface currents, and the surface potential density, with SSH contours superposed, for 4 days with variable wind conditions. The horizontal region of the plots encompasses the separated jet between 127°W, 124.5°W and 41.7°N, 42.7°N. The days and the corresponding wind conditions (Figure 8) are as follows: 0000 28 July, moderately strong winds relatively early in a several-day southward wind event; 0800 1 August, strong winds about 6 days into the same southward wind event; 0000 6 August, weak winds between southward wind events; 0000 13 August, strong winds about 6 days into a second strong southward wind event. Also plotted in Figure 17 is a measure of the flow imbalance:

$$\epsilon = \frac{\partial(\nabla_h \cdot \mathbf{u})/\partial t}{f(|\zeta| + \overline{\langle\zeta^2\rangle^{1/2}})} \tag{5}$$

[*McWilliams*, 1985; cf. *Capet et al.*, 2008b, equation (16)], where $\nabla_h \cdot \mathbf{u} = u_x + v_y$ is the horizontal divergence of the surface velocity and $\zeta = v_x - u_y$ is the relative vorticity of the surface currents. The term $\overline{\langle\zeta^2\rangle^{1/2}}$, where the brackets represent a spatial average over the horizontal subregion shown and the overbar represents a time average over the period 26 July to 21 August, is added to avoid singular behavior at zeros of $\zeta$. Values of $|\epsilon| \ll 1$ indicate that the flow is essentially in balance, typically through a geostrophic or a more general gradient-wind balance. Values of $\epsilon = O(1)$ indicate that the flow is unbalanced.

[33] We look first at the fields for 0800 1 August, which correspond to the same time as the sections in Figures 14 and 15 and the horizontal fields in Figures 13 and 16. The $w$ field (Figure 17e) shows relatively small scale spatial variations along the jet with a wavelength of 20–30 km. These disturbances are found to propagate westward in the direction of the jet with a phase speed of about 25 km $d^{-1}$ (Figure 18) and reflect the presence of submesoscale instabilities in the surface layer of the jet. From the sections in

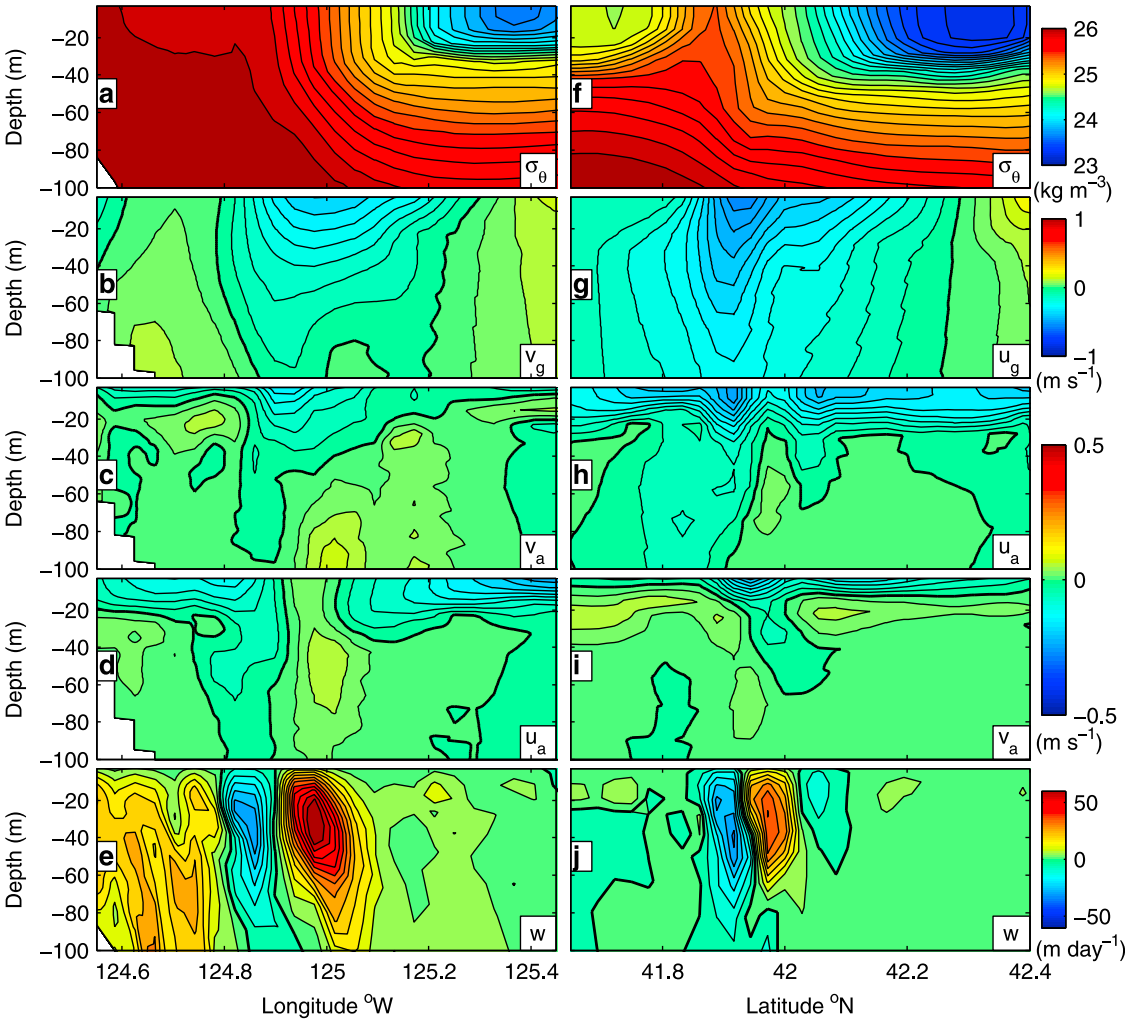


**Figure 14.** Cross-jet (a–e) near-coastal and (f–j) offshore sections at 0800 1 August: potential density (Figures 14a and 14f), geostrophic $v_g$ (Figure 14b), $u_g$ (Figure 14g), and ageostrophic $v_a$ (Figure 14c), $u_a$ (Figure 14h) components of along-jet velocity, ageostrophic component of the cross-jet velocity $u_a$ (Figure 14d), $v_a$ (Figure 14i), and vertical velocity $w$ (Figures 14e and 14j). Color contour intervals are 0.1 kg m$^{-3}$ for $\sigma_\theta$, 0.05 m s$^{-1}$ for ($u_g$, $v_g$), 0.025 m s$^{-1}$ for ($u_a$, $v_a$), and 5 m d$^{-1}$ for $w$. Bold isolines denote zero velocity. The near-coastal cross-jet section is along 42.63°N, and the offshore section is along 126°W (see Figure 13).

Figure 14, the magnitudes of the vertical velocities in these disturbances can reach values of 60 m d$^{-1}$ at the near-coastal section and 40 m d$^{-1}$ at the offshore section. The corresponding spatial variations in the surface vorticity field $\zeta$ (due mostly to the vorticity in the geostrophic surface currents), in the surface potential density field, and in the SSH field are relatively smooth, reflecting the larger-scale jet structure, and do not give strong indications of variability on the smaller scales of the vertical velocity disturbances. The $\epsilon$ field has a spatial structure clearly related to that of the $w$ field, with magnitudes reaching around 0.5 in the regions of the large vertical velocities. Values of $\epsilon$ of that magnitude clearly indicate that these small-scale disturbances are not in either geostrophic or gradient-wind balance and that they are unbalanced. Note that evidence for the presence of the instabilities can be seen in the 1 August horizontal field of TKE (Figure 16) through the small-scale fluctuations of TKE in the jet. In those fluctuations, the TKE values are generally reduced in the regions of upwelling velocities, as shown in the offshore section (Figures 14 and 15).

[34] During weak wind conditions on 6 August, the $\zeta$ field (Figure 17j) shows strong along-jet perturbations with a wave-like structure and an along-jet scale of about 50–70 km. These perturbations, also present in the surface potential density field, propagate along the jet with a phase speed of 25–30 km d$^{-1}$. In contrast to the behavior on 1 August, the $w$ field (Figure 17i) along the jet exhibits weaker variability and smaller magnitudes. The largest magnitudes of $w$ are associated with downwelling and are found near the crests of the along-front instabilities (Figure 17k), where the curvature of the SSH field is locally large. The $\epsilon$ values are relatively low (Figure 17l) with two spots of increased values, also near the crests. The instabilities present on this day appear to have a different dynamical structure than those found during strong winds on 1 August and, from the $\epsilon$ fields, to be essentially balanced.

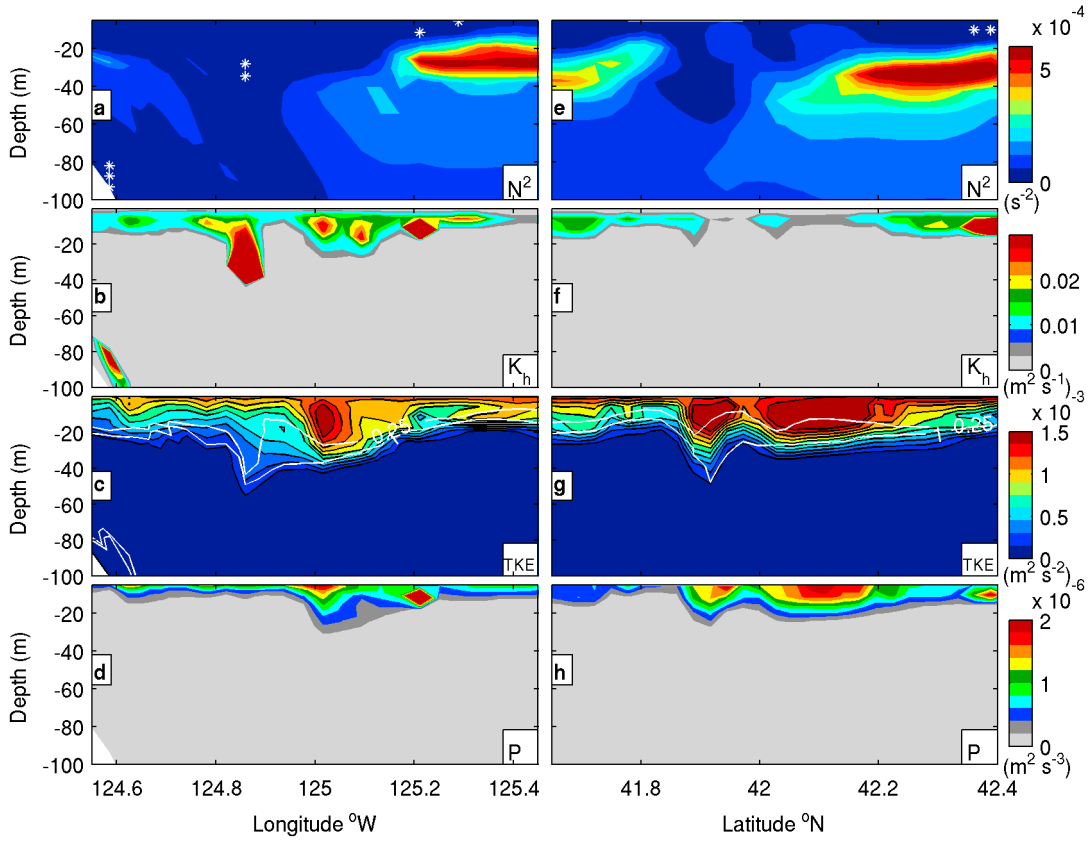


**Figure 15.** Cross-jet (a–d) near-coastal and (e–h) offshore sections at 0800 1 August: buoyancy frequency $N^2$ (Figures 15a and 15e), vertical turbulent diffusivity coefficient $K_h$ (Figures 15b and 15f), turbulent kinetic energy in color, Richardson number $Ri = N^2/S^2$ in white contours (Figures 15c and 15g), and shear production $P = K_m S^2$ (Figures 15d and 15h). Negative values of $N^2$ are denoted by white stars. The near-coastal cross-jet section is along 42.63°N, and the offshore section is along 126°W (see Figure 13).

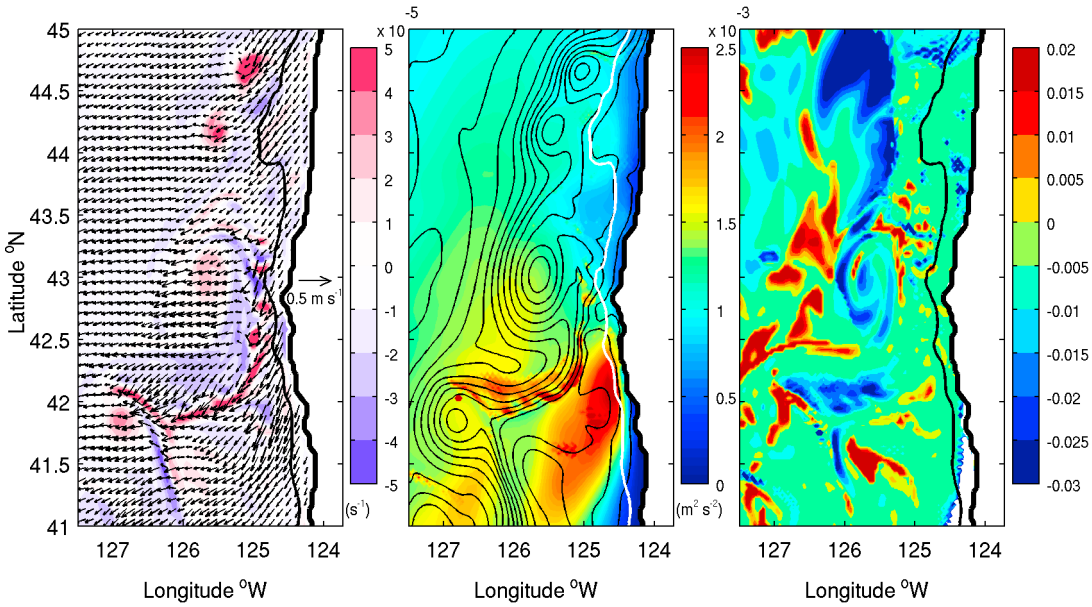


**Figure 16.** (left) Ageostrophic component of the surface current $\mathbf{u_a}$ in vectors and relative vorticity of geostrophic surface current $\zeta_g$ in color, (middle) maximum of the turbulent kinetic energy in the upper 25 m in color and SSH in contours, and (right) maximum of the stability function $G_h$ in the upper 25 m at 0800 1 August. The solid black and white lines show the 200 m isobath.

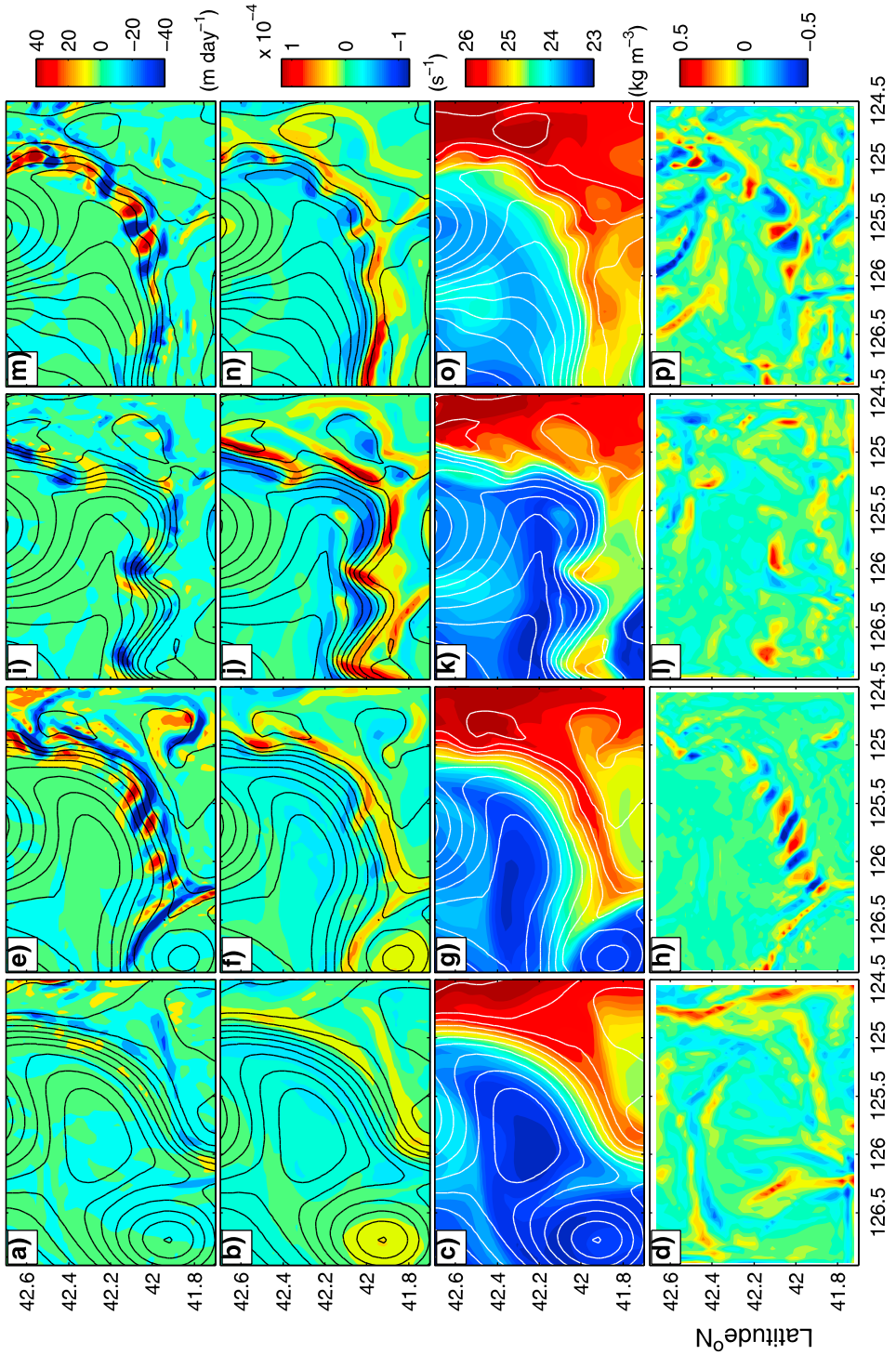


**Figure 17.** (a, e, i, m) Vertical velocity at 25 m depth $w$, (b, f, j, n) relative vorticity of the surface current $\zeta$, (c, g, k, o) surface potential density $\sigma_\theta$, and (d, h, l, p) a measure of the imbalance $\epsilon$ [see (5) in section 4.5] for the area around the separated jet at 0000 28 July (Figures 17a–17d), 0800 1 August (Figures 17e–17h), 0000 6 August (Figures 17i–17l), and 0000 13 August (Figures 17m–17p). Black and white contours show the SSH with contour intervals 0.02 m.

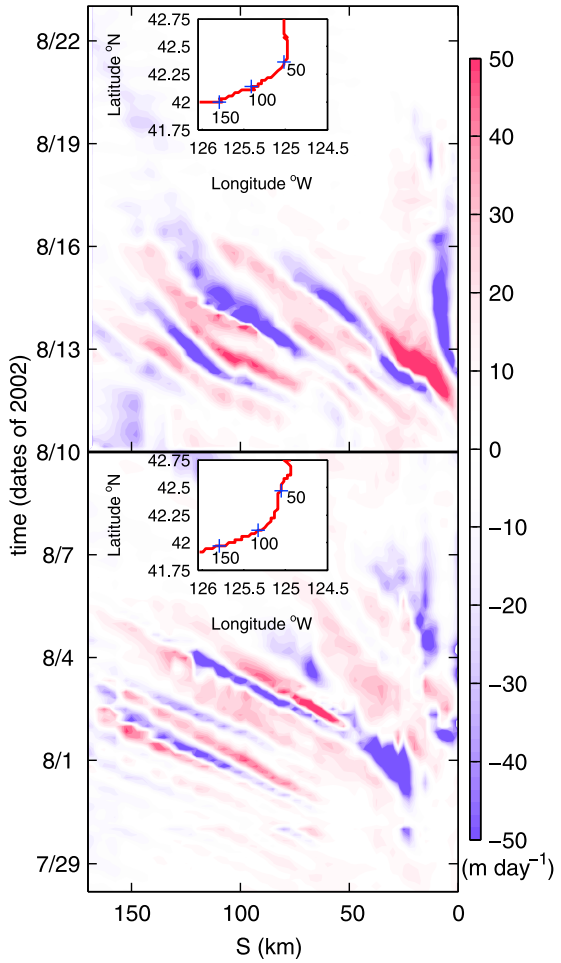


**Figure 18.** Hovmöller diagrams of $w$ at 25 m sampled along the jet path (shown in small windows), as determined from the mean location of the maximum in $|\nabla_h \rho|$, for two time intervals of instability occurrence.

[35] During the second strong wind event on 13 August, the small-scale, unbalanced instabilities are again present with substantial fluctuations in the $w$ field, accompanied by related variations in $\epsilon$ (Figure 17p), propagating along the jet (Figure 18), similar to those on 1 August. Fluctuations in the surface vorticity field and in the surface potential density field, however, are larger than those on 1 August, with some resemblance to those present during weak winds on 6 August. Two days after this event on 15 August, the small-scale, unbalanced instabilities decayed (not shown here) and the vorticity and density fields became very much like those on 6 August, with similar disturbances of wave-like structure. Thus, there are some indications that the small-scale, unbalanced instabilities may subsequently evolve into the larger-scale, balanced instabilities.

[36] To examine the generation and propagation of the small-scale, unbalanced instabilities shown in Figures 17e–17m, we construct a Hovmöller diagram of the time-dependent vertical velocities $w$ at 25 m depth, sampled along the mean path of maximum density gradient $|\nabla_h \rho|$ representing the jet axis, for two time intervals when those instabilities are present: 28 July to 9 August, and 10–22 August (Figure 18). During the first time interval, strong instabilities, identified by large-magnitude vertical velocities (up to 60 m $d^{-1}$), start to develop on 30 July. They propagate along the jet path and stay in the subdomain until 4 August. Most of the instabilities during that interval originate between 50 and 100 km from the start point of the jet path in a region where the jet is still mainly flowing toward the south before turning offshore (see the plot of the mean path in Figure 18). If we consider individual perturbations, then the lifetime of a perturbation, defined as the time when the magnitude of $w$ is greater than 25 m $d^{-1}$, can be estimated to be around 3 days and the distance traveled to be around 75 km, which gives an average propagation speed of 25 km $d^{-1}$. During the second time period of instability occurrence, more instabilities originate closer to the start point of the jet path, and not all of them travel all the way to the offshore part of the subdomain. Instabilities are present in the subdomain from 11 to 17 August. They are characterized by larger vertical velocities, up to 100 m $d^{-1}$, longer lifetimes around 4 days, and smaller average propagation speeds of 18 km $d^{-1}$.

[37] To further examine the time-dependent relationship of the relatively large fluctuations in vertical velocity that contribute to the horizontal fields of mean and standard

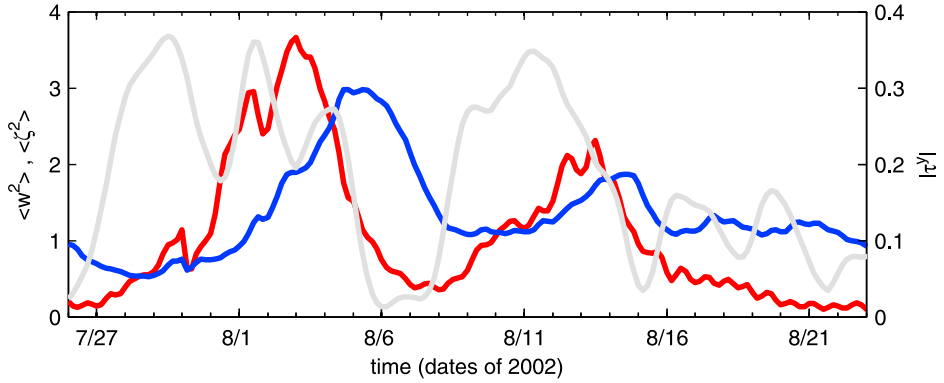


**Figure 19.** Time-series plots of the spatial average, denoted by brackets, over the region around the separated jet shown in Figure 17 of $\langle w^2 \rangle$ at 25 m ($m^2\ s^{-2} \times 10^{-8}$; red line) and surface $\langle \zeta^2 \rangle$ ($s^{-2} \times 5 \times 10^{-10}$; blue line). Also plotted is the corresponding time series of $|\tau^y|$ (N $m^{-2}$; gray line) calculated as in Figure 8.

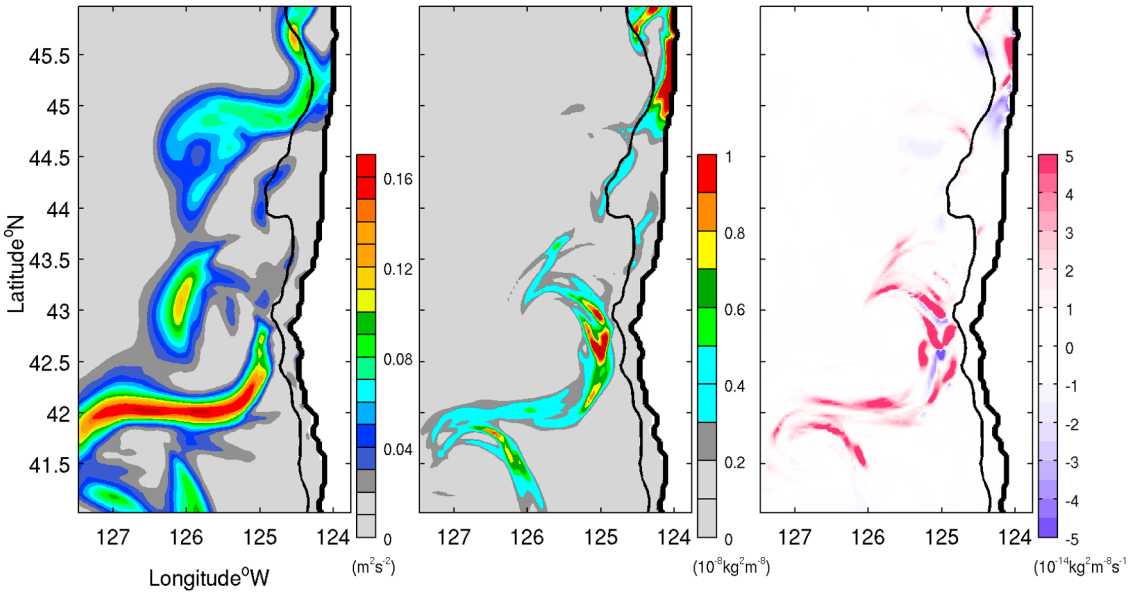


**Figure 20.** (left) Kinetic energy of the surface current, (middle) absolute value of the horizontal gradient of surface density squared $|\nabla_h \rho|^2$, and (right) the frontogenesis function $F_s$ (7), averaged over 26 July to 21 August. The solid black line shows the 200 m isobath.

deviation of $w$ in Figure 10, with the occurrence of the submesoscale instabilities, we calculate the spatial average (again denoted by brackets) of the vertical velocity squared $\langle w^2 \rangle$ at 25 m depth and surface vorticity squared $\langle \zeta^2 \rangle$ over the subregion around the offshore separated jet shown in Figure 17. Those values, together with the magnitude of wind stress, are plotted as time series for 26 July to 22 August in Figure 19. Two events of large $\langle w^2 \rangle$ occur, on 3 and 13 August, respectively. These events coincide with the presence of the small-scale, unbalanced instabilities. The lagged relation of the larger values of $\langle w^2 \rangle$ with larger values of the southward wind stress is clear. (The maximum correlation coefficient of $\langle w^2 \rangle$ and $|\tau^y|$ is 0.62 at a lag of 2 days.) The two events of large $\langle w^2 \rangle$ are followed by increased $\langle \zeta^2 \rangle$ with about 2 days lag. This evidently reflects the weakening of the small-scale, unbalanced instabilities and the subsequent growth of, or evolution into, the larger-scale balanced instabilities, characterized by substantial fluctuations in vorticity.

### 4.6. Frontogenesis Along the Separated Jet

[38] To assess the frontogenesis along the separated jet, we use the frontogenesis function $F$ following the work of *Capet et al.* [2008b]:

$$\frac{D|\nabla_h \rho|^2}{Dt} = 2F, \tag{6}$$

where $|\nabla_h \rho|^2 = (\partial\rho/\partial x)^2 + (\partial\rho/\partial y)^2$ is the absolute value of surface density gradient squared. Horizontal fields of the kinetic energy of surface currents KE = 0.5 $(u^2 + v^2)$, $|\nabla_h \rho|^2$, and the part of $F$ due to horizontal advection [*Hoskins*, 1982; *Capet et al.*, 2008b],

$$F_s = -\left[\frac{\partial u}{\partial x}\left(\frac{\partial \rho}{\partial x}\right)^2 + \frac{\partial v}{\partial y}\left(\frac{\partial \rho}{\partial y}\right)^2 + \left(\frac{\partial v}{\partial x} + \frac{\partial u}{\partial y}\right)\frac{\partial \rho}{\partial x}\frac{\partial \rho}{\partial y}\right], \tag{7}$$

averaged in time over the 27 day period 26 July to 21 August, are shown in Figure 20. The structure of the surface kinetic energy field is remarkable in that by far the largest values over the entire domain are concentrated in the region of the separated jet offshore south of Cape Blanco. Dynamically consistent large values of the absolute value of the horizontal gradient of the surface density squared $|\nabla_h \rho|^2$ are also found concentrated along the jet in the same region. However, the largest values of $|\nabla_h \rho|^2$ occur near the coast between 42.5°N and 43°N, where the jet is still flowing south in the general direction of the wind stress. The large values of $|\nabla_h \rho|^2$ in the separated jet are clearly related to the concentrated large mean values of the frontogenesis function $F_s$ found in the same region. In particular, there is an obvious match between the increased magnitudes of both fields in the jet near the coast between 42.5°N and 43°N. It appears that frontogenesis processes related to the CTZ flow fields play a major role in establishing the structure and intensity of the separated jet. In the nearshore southward flowing part of the jet, frontogenesis processes, intensified by the along-jet wind stress, contribute directly to the development of the FSC. In the offshore part of the jet, frontogenesis processes influence the structure of the jet and thus affect the behavior of the submesoscale instabilities. Consequently, in both parts of the jet, frontogenesis processes play a role in the maintenance of the concentrated large mean and RMS vertical velocities shown in Figure 10.

[39] To document one additional aspect of the behavior of the vertical velocities, regarding possible differences in the maximum magnitudes of the down- and upwelling velocities, we calculate probability density functions of the extreme positive and negative values of $w$ over the top 80 m depth and over the time period 26 July to 21 August (Figure 21). Two horizontal regions are selected: one for the near-coastal part of the jet, where it is flowing southward in the direction of the wind stress, and one for the offshore part, where it flows

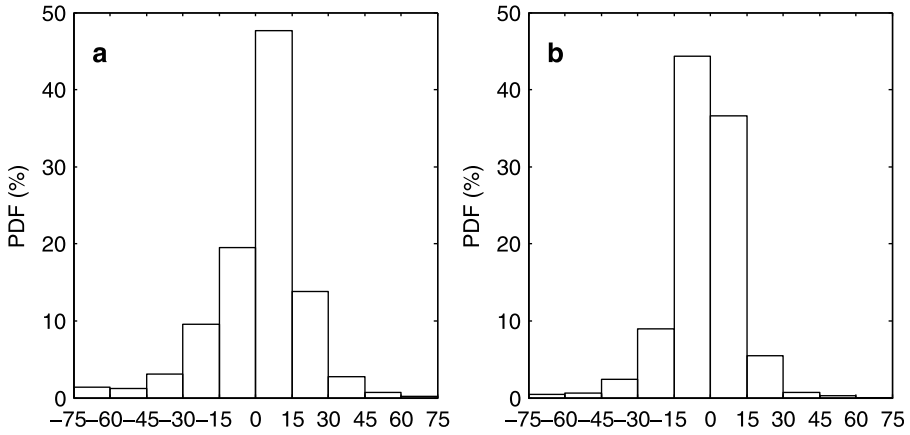


**Figure 21.** Histogram of the extreme positive and negative values of the vertical velocity $w$ over the top 80 m depth across the coastal jet in its (a) near-coastal and (b) offshore parts. The near-coastal part of the jet for this sampling extends from 42.2°N to 43°N and the offshore part extends from 125.7°W to 126.3°W. The sampling is made in a 36 km band, centered along the jet axis, defined here by the mean location of the maximum surface velocity, and the integration interval is from 26 July to 21 August.

westward. The near-coastal region extends from 42.3°N to 43°N and includes all values along east-west grid lines 18 km on either side of the jet axis, defined by the mean location of the maximum surface velocity. The offshore section extends from 125.7°W to 126.3°N and includes all values along north-south grid lines 18 km on either side of the jet axis. From Figure 21a we can see that in the near-coastal region, where the down-front winds evidently contribute to an increase in the absolute values of surface density gradients (Figure 20) and to an intensification of the accompanying FSC (Figure 10), the positive upwelling velocities clearly have more occurrences of larger magnitude than do the negative downwelling velocities. Thus, in this region we find typically stronger upwelling velocities and weaker downwelling velocities. Consistent with that result, stronger upwelling velocities are evident in the instantaneous near-coastal section in Figure 14. The behavior differs, however, in the offshore region (Figure 21b), where the downwelling velocities have more occurrences of larger magnitude than the upwelling velocities. Thus, in the offshore region, where the wind stress is normal to the direction of the jet and where the more energetic vertical circulation appears to be primarily associated with time-dependent, submesoscale instabilities, we find evidence for typically stronger downwelling velocities. That general behavior is also consistent with the model results of *Capet et al.* [2008b] and with theoretical results [*Hoskins*, 1982] concerning the FSC associated with frontogenesis caused by larger-scale horizontal deformation fields.

## 5. Discussion

[40] The phenomenon of nonlinear interaction between effects of a geostrophic flow and a wind stress applied to a surface Ekman layer has been studied in a number of papers [*Stern*, 1965; *Niiler*, 1969; *Thomas and Rhines*, 2002; *Thomas and Lee*, 2005; *Pedlosky*, 2008]. *Lee et al.* [1994] used a two-dimensional numerical model to study the case when a spatially uniform wind is applied both along and across a geostrophically balanced jet. They reported secondary circulation that is created as a result of a nonlinear interaction between the jet and the wind-driven flow in the Ekman layer. In that study (as well as the aforementioned studies), an expression similar to equation (4) for the Ekman transport, $M_E$, was used. They found that when the wind blows perpendicular to the jet the secondary circulation is 50% weaker than when the wind blows parallel to the jet, with upward vertical advection on the upwind side of the jet ($\zeta < 0$) and downward advection on downwind side ($\zeta > 0$). *Lee and Niiler* [1998] modeled the ocean response to uniform wind stress forcing over geostrophically balanced eddies. Their results for the mean secondary circulation were consistent with the features found in the work of *Lee et al.* [1994]. *Centurioni et al.* [2008] used surface drifter data, satellite SSH measurements, and NCEP reanalysis winds to map the time-averaged 15 m depth geostrophic velocity field in the CCS. The resultant mean circulation and eddy energy distributions were found to be in reasonable agreement with ROMS CCS model results of *Marchesiello et al.* [2003]. Analysis of the time-averaged near-surface ageostrophic velocity field in the ROMS CCS solutions showed behavior similar to that found in the work of *Lee and Niiler* [1998] and thus was argued to be associated with the nonlinear interaction of Ekman dynamics with the geostrophic vorticity field. *Pedlosky* [2008], in an analytical study for a homogeneous fluid, determined the nonlinear effects of geostrophic vorticity $\zeta_g$ and wind stress curl on the Ekman layer thickness. The importance of accounting for the Ekman layer depth for calculations of surface velocity from satellite SSH measurements was noted in section 4.4. *Thomas and Lee* [2005] studied the effect of strong winds blowing in the direction of a frontal jet on frontogenesis and found that the frontogenesis secondary circulation, characterized by subduction on the dense side of the front and upwelling along the frontal interface, is intensified. The results of that study appear especially relevant to the behavior found here in the near-coastal region of the separated jet where it flows southward in the direction of the

wind stress. Our simulations of the 3-D dynamics of the jet in the Oregon CTZ, however, contain a more complicated set of time- and space-dependent dynamical processes than those represented in most of these idealized model investigations. Additional process-oriented studies in a realistic CTZ environment would be useful.

[41] The behavior and the dynamics of circulation processes near the ocean surface have been addressed further in several recent studies [*Capet et al.*, 2008a, 2008b, 2008c; *Lapeyre and Klein*, 2006; *Lapeyre et al.*, 2006; *Klein et al.*, 2008; *Boccaletti et al.*, 2007; *Fox-Kemper et al.*, 2008; *Fox-Kemper and Ferrari*, 2008]. In particular, the subject of near-surface vertical exchange associated with submesoscale processes was discussed in a useful recent review paper by *Klein and Lapeyre* [2009]. The previous results of most relevance here are those of *Capet et al.* [2008a, 2008b, 2008c], where the dynamics of near-surface submesoscale processes in an idealized eastern boundary current oceanic regime with steady wind forcing was investigated. In particular, *Capet et al.* [2008b] found evidence for more intense FSC in fronts oriented in the downwind direction, consistent with the results of *Thomas and Lee* [2005] and in agreement with the behavior found here in the near-coastal southward flowing part of the separated coastal jet. *Capet et al.* [2008b] also found evidence for frontogenesis processes associated with regions of large surface density gradients, similar to the behavior shown here in Figure 20. In addition, *Capet et al.* [2008b] found occurrences of submesoscale instability growth and propagation along fronts with instability wavelengths of 20–30 km. The instabilities were characterized by spatial variations in the surface potential density $\sigma_\theta$ and by increases in magnitude of corresponding submesoscale surface vorticity $\zeta$ fluctuations. The small-scale, unbalanced instabilities found here (Figures 17 and 18) have similar spatial scales but appear to be characterized most strongly by substantial fluctuations in $w$, resulting in vigorous vertical exchange in the surface layer (Figure 14j), with relatively smaller variations in $\zeta$. Moreover, there is a clear relation between increased strength of the wind stress and occurrence of these instabilities (Figure 19). To what extent the development of these instabilities depends on the wind stress through resultant changes in the structure of the separated jet, on the increase in magnitude of the surface layer ageostrophic transport, or on their interaction is not clear from these simulations. Additional controlled process studies to address these questions would be useful. In contrast, the somewhat larger scale instabilities found on 6 August are characterized by substantial variations in surface $\zeta$ and $\sigma_\theta$ and by a larger degree of balance (Figures 17j–17l).

[42] We note that the primary differences in the results of our limited-time simulation of late-summer conditions, with realistic wind-stress forcing and realistic coastal topography, and those from the longer-time simulations of *Capet et al.* [2008a, 2008b, 2008c], with more idealized forcing and topography, is in the strong space- and time-dependent behavior found here. In particular, the significant spatial concentration of the near-surface ageostrophic vertical circulation processes in the region of the separated coastal jet off Cape Blanco (Figure 10) and the time-dependent behavior of that circulation in response to the wind-stress forcing (Figure 19), appears to identify potentially important components of realistic CTZ flow fields off Oregon and northern California.

## 6. Summary

[43] On the basis of comparisons with different types of data, our 3-D nonlinear model describes the dynamics both on the shelf and in the CTZ off Oregon qualitatively correctly. Comparisons with currents at midshelf moorings indicate that the model reproduces both depth-averaged and baroclinic dynamics on the shelf. The modeled SST front evolution is consistent with satellite SST fields showing the major feature of summertime Oregon CTZ dynamics, such as the separation of the coastal jet near Cape Blanco. HF-radar measurements of surface currents (Figure 6) provide evidence that the observed jet that separates off Cape Blanco is as energetic as the modeled separating jet with maximum speeds reaching 0.6–0.8 m $s^{-1}$. Lagrangian analysis reveals characteristic flow patterns over the shelf and in the CTZ off Oregon, particularly separated jets near Heceta Bank and Cape Blanco.

[44] The behavior of near-surface circulation in the CTZ off Oregon during a late-summer 27 day time period, 26 July to 21 August, was investigated. Significant vertical velocities were found concentrated in the region of the separated jet south of Cape Blanco. In the near-coastal part of the separated jet, where it was flowing southward in the direction of the winds, the wind stress appeared to intensify the frontogenesis secondary circulation. The associated instantaneous vertical velocities were as large as 100 m $d^{-1}$. In the offshore part of the separated jet, where it was flowing westward, the energetic vertical velocities were primarily associated with time-dependent submesoscale instabilities. Those instabilities were present during strong southward wind events. They propagated in the direction of the jet with wavelengths of 20–30 km and propagation speeds of 18–25 km $d^{-1}$. The larger vertical velocities were typically 50 m $d^{-1}$.

[45] As a next step, it would be useful to extend these analyses to a coupled biophysical model to see how the surface-layer processes within the jet affect biological variability.

[46] **Acknowledgments.** This is contribution number 658 of the U.S. GLOBEC program, jointly funded by the National Science Foundation and the National Oceanic and Atmospheric Administration. We gratefully acknowledge support for this research by the U.S. GLOBEC-NEP project and by the Cooperative Institute for Oceanographic Satellite Studies, which is supported by the National Oceanic and Atmospheric Administration, both through award NA03NES4400001, and the Office of Naval Research Physical Oceanography project, award N000140810942. The GLOBEC-NEP mooring data at Coos Bay and Rogue River were provided by B.M. Hickey and S.R. Ramp. Data for the NH10 GLOBEC mooring and HF-radar measurements were provided by P.M. Kosro. Satellite information on SST was provided by P.T. Strub. Data on SeaSoar density measurements were provided by J.A. Barth. The NCOM results were supplied by I. Shulman. We thank all the above investigators. We also thank S.R. Springer for the help in model setup and G.D. Egbert and R.N. Miller for thoughtful discussions. We are especially grateful to two anonymous reviewers for constructive and helpful comments that led to substantial positive revisions in an initial manuscript.

## References

Barth, J. A., and P. A. Wheeler (2005), Introduction to special section: Coastal advances in shelf transport, *J. Geophys. Res.*, *110*, C10S01, doi:10.1029/2005JC003124.

Barth, J. A., S. D. Pierce, and R. L. Smith (2000), A separating coastal upwelling jet at Cape Blanco, Oregon and its connection to the California current system, *Deep Sea Res., Part II*, *47*, 783–810.

Barth, J. A., S. D. Pierce, and T. J. Cowles (2005), Mesoscale structure and its seasonal evolution in the northern California current system, *Deep Sea Res., Part II*, *52*, 5–28.

Batchelor, G. K. (1967), *An Introduction to Fluid Dynamics*, 615 pp., Cambridge Univ. Press, New York.

Boccaletti, G., R. Ferrari, and B. Fox-Kemper (2007), Mixed layer instabilities and restratification, *J. Phys. Oceanogr.*, *37*, 2228–2250.

Brink, K. H., and T. J. Cowles (1991), The coastal transition zone program, *J. Phys. Oceanogr.*, *96*, 14,637–14,647.

Capet, X., J. C. McWilliams, M. J. Molemaker, and A. F. Shchepetkin (2008a), Mesoscale to submesoscale transition in the California current system. Part I: Flow structure, eddy flux, and observational tests, *J. Phys. Oceanogr.*, *38*, 29–43.

Capet, X., J. C. McWilliams, M. J. Molemaker, and A. F. Shchepetkin (2008b), Mesoscale to submesoscale transition in the California current system. Part II: Frontal processes, *J. Phys. Oceanogr.*, *38*, 44–64.

Capet, X., J. C. McWilliams, M. J. Molemaker, and A. F. Shchepetkin (2008c), Mesoscale to submesoscale transition in the California current system. Part III: Energy balance and flux, *J. Phys. Oceanogr.*, *38*, 2256–2269.

Castelao, R. M., and J. A. Barth (2007), The role of wind stress curl in jet separation at a cape, *J. Phys. Oceanogr.*, *37*, 2652–2671.

Centurioni, L. R., J. C. Ohlmann, and P. P. Niiler (2008), Permanent meanders in the California current system, *J. Phys. Oceanogr.*, *38*, 1690–1710.

Chapman, D. C. (1985), Numerical treatment of cross-shelf open boundaries in a barotropic coastal ocean model, *J. Phys. Oceanogr.*, *15*, 1060–1075.

Dewey, R. K., J. N. Moum, C. A. Paulson, D. R. Caldwell, and S. D. Pierce (1991), Structure and dynamics of a coastal filament, *J. Geophys. Res.*, *96*(C8), 14,885–14,907.

Di Lorenzo, E. (2003), Seasonal dynamics of the surface circulation in the Southern California current system, *Deep Sea Res., Part II*, *50*, 2371–2388.

Fairall, C. W., E. F. Bradley, J. E. Hare, A. A. Grachev, and J. B. Edson (2003), Bulk parameterization of air-sea fluxes: Updates and verification for the COARE algorithm, *J. Clim.*, *16*, 571–591.

Flather, R. A. (1976), A tidal model of the north-west European continental shelf, *Mem. Soc. R. Sci. Liege*, *6*, 141–164.

Fox-Kemper, B., and R. Ferrari (2008), Parameterization of mixed layer eddies. Part II: Prognosis and impact, *J. Phys. Oceanogr.*, *38*, 1166–1179.

Fox-Kemper, B., R. Ferrari, and R. W. Hallberg (2008), Parameterization of mixed layer eddies. Part I: Theory and diagnosis, *J. Phys. Oceanogr.*, *38*, 1145–1165.

Fu, L.-L., E. J. Christensen, C. A. Yamarone, M. Lefebvre, Y. Menard, M. Dorrer, and P. Escudier (1994), TOPEX/POSEIDON mission overview, *J. Geophys. Res.*, *99*(C12), 24,369–24,381.

Galperin, B., L. H. Kantha, S. Hassid, and A. Rosati (1988), A quasi-equilibrium turbulent energy model for geophysical flows, *J. Atmos. Sci.*, *45*, 55–62.

Gan, J., and J. S. Allen (2002), A modeling study of shelf circulation off northern California in the region of the Coastal Ocean Dynamics Experiment 2. Simulations and comparisons with observations, *J. Geophys. Res.*, *107*(C11), 3184, doi:10.1029/2001JC001190.

Haidvogel, D. B., J. Blanton, J. C. Kindle, and D. R. Lynch (2000), Coastal ocean modeling: Processes and real-time systems, *Oceanography*, *13*, 35–46.

Hodur, R. M. (1997), The Naval Research Laboratory's Coupled Ocean/Atmosphere Mesoscale Prediction System (COAMPS), *Mon. Weather Rev.*, *125*, 1414–1430.

Hoskins, B. J. (1982), The mathematical theory of frontogenesis, *Annu. Rev. Fluid Mech.*, *14*, 131–151.

Kadko, D. C., L. Washburn, and B. Jones (1991), Evidence of subduction within cold filaments of the northern California coastal transition zone, *J. Phys. Oceanogr.*, *96*, 14,909–14,926.

Kalnay, E., et al. (1996), The NCEP/NCAR 40-year reanalysis project, *Bull. Am. Meteorol. Soc.*, *77*, 437–471.

Klein, P., and G. Lapeyre (2009), The oceanic vertical pump induced by mesoscale and submesoscale turbulence, *Annu. Rev. Mar. Sci.*, *1*, 351–375.

Klein, P., B. Hua, G. Lapeyre, X. Capet, S. Le Gentil, and H. Sasaki (2008), Upper ocean turbulence from high-resolution 3D simulations, *J. Phys. Oceanogr.*, *38*, 1748–1763.

Kosro, P. M. (2003), Enhanced southward flow over the Oregon shelf in 2002: A conduit for subarctic water, *Geophys. Res. Lett.*, *30*(15), 8023, doi:10.1029/2003GL017436.

Kosro, P. M. (2005), On the spatial structure of coastal circulation off Newport, Oregon, during spring and summer 2001 in a region of varying shelf width, *J. Geophys. Res.*, *110*, C10S06, doi:10.1029/2004JC002769.

Lapeyre, G., and P. Klein (2006), Dynamics of the upper oceanic layers in terms of surface quasigeostrophy theory, *J. Phys. Oceanogr.*, *36*, 165–176.

Lapeyre, G., P. Klein, and B. Hua (2006), Oceanic restratification forced by surface frontogenesis, *J. Phys. Oceanogr.*, *36*, 1577–1590.

Lee, D., P. Niiler, A. Warn-Varnas, and S. Piacsek (1994), Wind-driven secondary circulation in ocean mesoscale, *J. Mar. Res.*, *52*, 371–396.

Lee, D.-K., and P. P. Niiler (1998), The inertial chimney: The near-inertial energy drainage from the ocean surface to the deep layer, *J. Geophys. Res.*, *103*(C4), 7579–7591.

Marchesiello, P., J. C. McWilliams, and A. Shchepetkin (2001), Open boundary conditions for long-term integration of regional oceanic models, *Ocean Modell.*, *3*, 1–20.

Marchesiello, P., J. C. McWilliams, and A. Shchepetkin (2003), Equilibrium structure and dynamics of the California current system, *J. Phys. Oceanogr.*, *33*, 753–783.

Maturi, E., A. Harris, C. Merchant, J. Mittaz, B. Potash, W. Meng, and J. Sapper (2008), NOAA's sea surface temperature products from operational geostationary satellites, *Bull. Am. Meteorol. Soc.*, *89*, 1877–1888.

McWilliams, J. C. (1985), A uniformly valid model spanning the regimes of geostrophic and isotropic, stratified turbulence: Balanced turbulence, *J. Atmos. Sci.*, *42*, 1773–1774.

Mellor, G. L., and T. Yamada (1982), Development of a turbulence closure model for geophysical fluid problems, *Rev. Geophys.*, *20*, 851–875.

National Geophysical Data Center (NGDC) (1988), Digital relief of the surface of the Earth, *Data Announce. 88-MGG-02*, NOAA, Boulder, Colo.

Niiler, P. P. (1969), On the Ekman divergence in an oceanic jet, *J. Geophys. Res.*, *74*(28), 7048–7052.

Paduan, J. D., P. M. Kosro, and S. M. Glenn (2004), A national coastal ocean surface current mapping system for the United States, *Mar. Technol. Soc. J.*, *38*, 102–108.

Pedlosky, J. (2008), On the weakly nonlinear Ekman layer: Thickness and flux, *J. Phys. Oceanogr.*, *38*, 1334–1339.

Ramp, S. R., and F. L. Bahr (2008), Seasonal evolution of the upwelling process south of Cape Blanco, *J. Phys. Oceanogr.*, *38*, 3–28.

Samelson, R., P. Barbour, J. Barth, S. Bielli, T. Boyd, D. Chelton, P. Kosro, M. Levine, E. Skyllingstad, and J. Wilczak (2002), Wind stress forcing of the Oregon coastal ocean during the 1999 upwelling season, *J. Geophys. Res.*, *107*(C5), 3034, doi:10.1029/2001JC000900.

Saraceno, M., P. T. Strub, and P. M. Kosro (2008), Estimates of sea surface height and near-surface alongshore coastal currents from combinations of altimeters and tide gauges, *J. Geophys. Res.*, *113*, C11013, doi:10.1029/2008JC004756.

Shchepetkin, A. F., and J. C. McWilliams (2003), A method for computing horizontal pressure-gradient force in an oceanic model with a nonaligned vertical coordinate, *J. Geophys. Res.*, *108*(C3), 3090, doi:10.1029/2001JC001047.

Shchepetkin, A. F., and J. C. McWilliams (2005), The regional ocean modeling system: A split-explicit, free-surface, topography-following-coordinate oceanic model, *Ocean Modell.*, *9*, 347–404, doi:10.106/j.oceanmod.2004.08.002.

Shulman, I., J. C. Kindle, S. deRada, S. C. Anderson, B. Penta, and P. J. Martin (2004), Development of a hierarchy of nested models to study the California current system, in *Estuarine and Coastal Modeling: Proceedings of the 8th International Conference on Estuarine and Coastal Modeling*, edited by L. Malcolm and P. E. Spaulding, pp. 74–88, Am. Soc. of Civ. Eng., Reston, Va.

Shulman, I., J. Kindle, P. Martin, S. deRada, J. Doyle, B. Penta, S. Anderson, F. Chavez, J. Paduan, and S. Ramp (2007), Modeling of upwelling/relaxation events with the Navy Coastal Ocean Model, *J. Geophys. Res.*, *112*, C06023, doi:10.1029/2006JC003946.

Springer, S. R., R. M. Samelson, J. S. Allen, G. D. Egbert, A. L. Kurapov, R. N. Miller, and J. C. Kindle (2009), A nested grid model of the Oregon coastal transition zone: Simulations and comparisons with observations during the 2001 upwelling season, *J. Geophys. Res.*, *114*, C02010, doi:10.1029/2008JC004863.

Stern, M. E. (1965), Interaction of a uniform wind stress with a geostrophic vortex, *Deep Sea Res.*, *12*, 355–367.

Strub, P. T., P. M. Kosro, and A. Huyer (1991), The nature of the cold filaments in the California current system, *J. Phys. Oceanogr.*, *96*, 14,743–14,768.

Strub, P. T., H. P. Batchelder, and T. J. Weingartner (2002), U.S. GLOBEC Northeast Pacific Program: Overview, *Oceanography*, *15*, 30–35.

Thomas, L. N., and C. M. Lee (2005), Intensification of ocean fronts by down-front winds, *J. Phys. Oceanogr.*, *35*, 1086–1102.

Thomas, L. N., and P. B. Rhines (2002), Nonlinear stratified spin-up, *J. Fluid Mech.*, *473*, 211–244.

Washburn, L., D. C. Kadko, B. H. Jones, T. Hayward, P. M. Kosro, T. P. Stanton, S. Ramp, and T. Cowles (1991), Water mass subduction and the transport of phytoplankton in a coastal upwelling system, *J. Phys. Oceanogr.*, *96*, 14,927–14,946.

Wijesekera, H. W., J. S. Allen, and P. A. Newberger (2003), Modeling study of turbulent mixing over the continental shelf: Comparison of turbulent closure schemes, *J. Geophys. Res.*, *108*(C3), 3103, doi:10.1029/2001JC001234.

J. S. Allen, A. O. Koch, and A. L. Kurapov, College of Oceanic and Atmospheric Sciences, Oregon State University, Corvallis, OR 97331, USA. (akoch@coas.oregonstate.edu)